










Milliarcsecond structure and variability of methanol maser emission in three high-mass protostars

A. Aberfelds,¹   A. Bartkiewicz,²  M. Szymczak,²  J. Šteinbergs,¹  G. Surcis,³  A. Kobak,² 
M. Durjasz²  and I. Shmeld¹ 

¹Engineering Research Institute "Ventspils International Radio Astronomy Center", Ventspils University of Applied Sciences, Inženieru Str. 101, Ventspils, LV-3601, Latvia

²Institute of Astronomy, Faculty of Physics, Astronomy and Informatics, Nicolaus Copernicus University, Grudziadzka 5, 87-100 Torun, Poland

³INAF – Osservatorio Astronomico di Cagliari, Via della Scienza 5, I-09047 Selargius, Italy

Accepted XXX. Received YYY; in original form ZZZ

ABSTRACT

The variability study of 6.7 GHz methanol masers has become a useful way to improve our understanding of the physical conditions in high-mass star-forming regions. Based on the single-dish monitoring using the Irbene telescopes, we selected three sources with close sky positions. We imaged them using the European Very Long Baseline Interferometer Network and searched available data on VLBI archives to follow detailed changes in their structures and single maser spot variability. All three targets show a few groups of maser cloudlets of a typical size of 3.5 mas and the majority of them show linear or arched structures with velocity gradients of order $0.22 \text{ km s}^{-1} \text{ mas}^{-1}$. The cloudlets and overall source morphologies are remarkably stable on time scales of 7–15 yr supporting a scenario of variability due to changes in the maser pumping rate.

Key words: masers – stars: massive – instrumentation: interferometers – stars: formation – astrometry

1 INTRODUCTION

The formation of high-mass stars remains an important topic in modern astrophysics, as it is still not yet clear how a star obtains its final mass. It is believed that an embedded protostar can acquire the mass required to evolve into a massive star by either a global collapse or competitive accretion (e.g. Zinnecker & Yorke 2007, for review). High-mass star-forming regions (HMSFRs) are challenging for observational study due to their large distance, obscuration by dust clouds and fast evolution. Our ability to make significant progress in this field has been reinforced by the observations of methanol masers, especially the 6.7 GHz transition, whose spectral features are very bright and compact. The 6.7 GHz maser emission is primarily a unique signpost of HMSF sites (e.g. Menten 1991) and powerful tools to determine the trigonometric parallaxes (e.g. Rygl et al. 2010; Reid et al. 2019). High angular resolution observations allow us to measure the size and orientation of accretion disks, their kinematics and structure (e.g. Sanna et al. 2010a,b, 2017; Moscadelli et al. 2011a; Sugiyama et al. 2014). Long-term monitoring of the 6.7 GHz methanol masers has turned out to be an unexpectedly powerful tool for identifying accretion outbursts (Fujisawa et al. 2015; Szymczak et al. 2018; MacLeod et al. 2018; Burns et al. 2020).

A few detailed studies have been performed with the very-long baseline interferometry (VLBI) technique. Imaging maser emission at a milliarcsecond (mas) scale shows a variety of structures. The maser emission is frequently located along lines or arcs, sometimes with velocity gradients indicating the presence of edge-on discs (Norris et al. 1993; Minier et al. 2000; Dodson et al. 2004). Elliptical or ring-like morphologies observed in several sources (Bartkiewicz

et al. 2005, 2009, 2014, 2016; Fujisawa et al. 2014a) can arise from inclined or face-on rotating discs. Bartkiewicz et al. (2016) reported that almost half had a complex structure in a sample of 63 objects. A similar result was achieved by Fujisawa et al. (2014a).

Multi-epoch observations allow us to estimate the proper motions of single maser clouds and provide valuable information. For example, in G16.59–0.05 the bipolar distribution of 6.7 GHz maser line-of-sight velocities was associated with a rotating disk or toroid around a central mass of about $35 M_{\odot}$ (Sanna et al. 2010a). The velocity field of methanol masers can be explained in terms of a composition of slow (4 km s^{-1}) motion of radial expansion and rotation about an axis approximately parallel to the jet in the vicinity of massive young stars (e.g., Sanna et al. 2010b, Moscadelli et al. 2011a).

Long-term single-dish maser studies have found two different kinds of the variability of the 6.7 GHz methanol maser line: flaring and gradual (including periodic) changes of flux densities (e.g., Goedhart et al. 2004; Szymczak et al. 2018). Known variability periods range from 24 to 600 days and are seen in some or all features. Additionally phase-lags between individual features are also noticed (Goedhart et al. 2004; Goedhart et al. 2014; Fujisawa et al. 2014b and Szymczak et al. 2016). What causes the variability of 6.7 GHz methanol masers is still a topical field of research. Caswell et al. (1995) suggested that the maser variations are due to changes in the gain path length caused by large-scale motions. A strong correlation of maser and infrared flux densities was observed in the periodic 6.7 GHz sources (e.g. Olech et al. 2020, 2022; Kobak et al. 2023) indicates that the pumping rate plays a dominant role. Extraordinarily outbursts of the methanol masers in S255IR–NIRS3 and G358.93–0.03 are powered by accretion bursts (Caratti o Garatti et al. 2017; Stecklum et al. 2021).

* E-mail: artis.aberfelds@venta.lv

A combination of single-dish monitoring and detailed morphology analyses employing the VLBI technique mounts a convincing argument that most of the observed variability is caused by changes in maser pumping rates, furthermore implying the importance of infrared variability (Szymczak et al. 2014; Olech et al. 2019 and Durjasz et al. 2019).

The Irbene programme of 6.7 GHz methanol maser monitoring, which started in 2016, includes 41 targets from the Torun methanol maser catalogue (Szymczak et al. 2012). The sources were selected based on their declination above -10° and their maser flux density (>5 Jy). The main aim was to study the variability of 6.7 GHz methanol masers with particular attention to bursting episodes. Observation intervals were targeted every five days for all sources and daily for some exciting sources during their most active periods (Aberfelds et al. 2018). This paper presents results from the European VLBI Network¹ in order to: i) map the milliarcsecond structure of the emission of three sources with different variability behaviour, ii) identify maser groups responsible for the flux density changes seen in the single-dish spectra, and iii) put constraints on variability mechanisms going on around these high-mass young stars. Preliminary result for the source G78.122+3.633 was reported in Aberfelds et al. (2021).

2 TARGETS

Three 6.7 GHz methanol maser sources from the Irbene monitoring list were selected for VLBI observations as showing noticeable variability in 2018-2019. They were characterised by steady rise/decline of some features, moderate flares and fluctuations on timescales of a few months and years. The objects for VLBI studies are: G78.122+3.633, G90.92+1.49 and G94.602-1.796 (hereafter G78, G90 and G94 abbreviations are used accordingly). Below, we present some of their properties relevant in the context of the paper.

G78 (also known as IRAS 20126+4104) is a well studied early B0.5 spectral class star with Keplerian disk around $\sim 7M_\odot$ protostar (Cesaroni et al. 1997). Moscadelli et al. (2011a) reported water maser jet structure based on 22 GHz VLBA data and two groups of methanol masers based on the 6.7 GHz EVN observations. Two methanol maser groups appeared at very similar and overlapping LSR velocity ranges, from -4.5 to 8.5 km s⁻¹. The blue-shifted one is likely associated with a rotating, narrow ring related to the circumstellar disk, while the second is tracing the disk material marginally entrained by the jet. The trigonometric parallax were measured using the water masers by Moscadelli et al. (2011a) and Nagayama et al. (2015) providing a mean value of 0.645 ± 0.030 mas, implying $1.64^{+0.30}_{-0.12}$ kpc (Reid et al. 2019). JVLA images show the 6.7 GHz methanol emission in the LSR velocity range of -8.4 to -4.7 km s⁻¹, distributed in over $\sim 0''.36 \times 0''.25$ area without any regularities (Hu et al. 2016).

G90. The methanol maser in this source was discovered by Szymczak et al. (2000). In the BeSSeL² survey the parallax was estimated to be 0.171 ± 0.031 mas based on the methanol 6.7 GHz line measurements implying the distance of $5.85^{+1.30}_{-0.90}$ kpc (Reid et al. 2019). Images from the JVLA show emission distributed over $\sim 0''.3 \times 0''.6$ area at the LSR velocity of -71.5 to -68.3 km s⁻¹ with a velocity gradient from S-W to N-E (Hu et al. 2016). They also found a

0.63 Jy continuum emission about $0''.15$ S-E of the maser, whereas BeSSeL detected only the brightest part of arched maser distribution of ~ 130 mas in size.

G94 (also known as V645 Cyg or AFGL2789) is a young stellar object (YSO) containing O7 spectral type star (Cohen 1977) with variable gas outflows (Clarke et al. 2006). A mean trigonometric parallax of 0.221 ± 0.013 mas estimated based on the water and methanol masers (Oh et al. 2010; Choi et al. 2014; Sakai et al. 2019) indicates a distance of $4.5^{+0.3}_{-0.2}$ kpc (Reid et al. 2019). Slysh et al. (2002) observed this source using EVN with 5 antennas in 1998 and 2000 at the 6.7 GHz maser transition. Their images show four groups of masers with an indication of a rotating disc, as it was noted by the authors. JVLA images show emission in LSR velocity range from -44.1 to -40.4 km s⁻¹, distributed over $\sim 0''.10 \times 0''.22$ area with a velocity gradient from N to S of the major emission (Hu et al. 2016). They also found a weak radio-continuum emission with an integrated flux of 0.42 Jy.

3 OBSERVATIONS

We conducted single-epoch observations of the methanol maser transition $5_1-6_0 A^+$ (rest frequency of 6668.51920 MHz) using the EVN towards three targets: G78, G90 and G94. Observations were carried out on 31 October 2019, and the basic observing parameters are summarized in Table 1. The eleven EVN antennas that took part in these observations, which lasted for 10 h, are Jodrell, Effelsberg, Medicina, Onsala, Torun, Westerbork, Yebes, Sardinia, Irbene and Tianma. The phase-referencing technique was used with the cycle time of 105 s+225 s between a phase calibrator and a target. In total, the on-source time on the targets was ~ 139 , 105 and 98 min, respectively. 3C345 was used as a fringe finder and bandpass calibrator. To increase the signal-to-noise ratio for the phase-reference sources, two correlator passes were used; one using all eight BBCs per polarization, with a bandwidth of 4 MHz each (corresponding to ~ 200 km s⁻¹), and 128 correlator channels per BBC; the other using only the single BBC per polarization containing the maser line and 2048 correlator channels. The latter had a spectral resolution of 1.95 kHz (~ 0.088 km s⁻¹). Both data sets were processed at the Joint Institute for VLBI ERIC (JIVE) with the SFXC correlator (Keimpema et al. 2015). The Astronomical Image Processing System (AIPS) was used for data calibration and reduction. The standard procedures for line observations were used and Effelsberg antenna was set as a reference. The synthesised beam of final images was typically 4 mas \times 3 mas as listed in Table 1. We created 1024 px \times 1024 px image cubes with a pixel size of 1 mas, so we searched the region of $1'' \times 1''$ for the emission. To measure the spot parameters, we used the AIPS task JMFIT which implements a 2D Gaussian fitting procedure. The spectra were extracted from the image cubes using the AIPS task ISPEC.

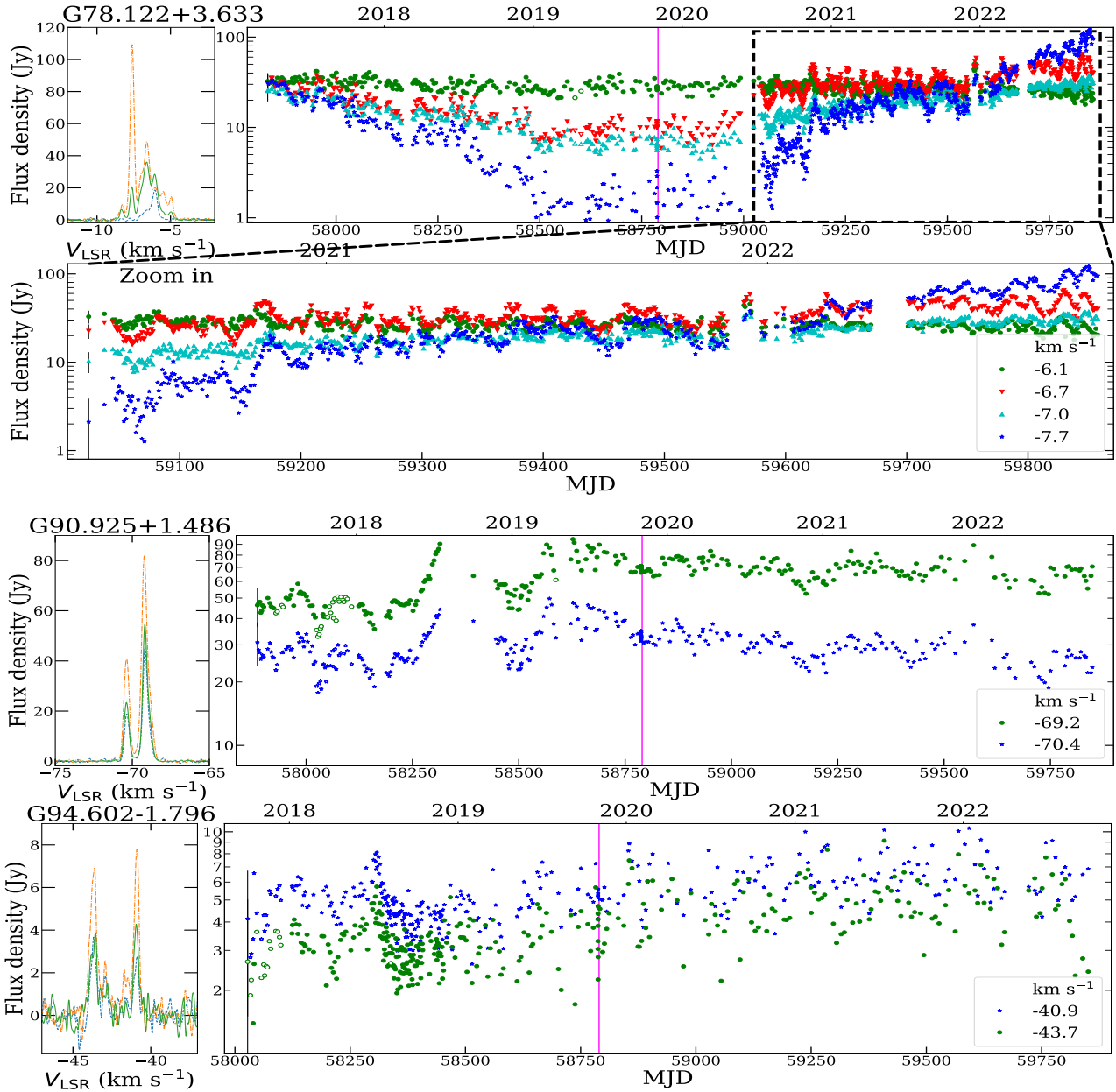
Moreover, the targets were observed from March 2017 to September 2022 as part of the maser monitoring project with the Irbene 32-m and 16-m radio telescopes in North-West Latvia. The vast majority ($\sim 96\%$) of presented data were obtained with the 16-m instrument. The observations were done at irregular time intervals of one day to one month with an average of 2.3, 6.5 and 5.2 d for G78, G90 and G94, respectively. The basic parameters of the instruments at 6.7 GHz transition are listed in Table 2. The data were reduced with MDPS package (Šteinbergs et al. 2021).

¹ The European VLBI Network is a joint facility of independent European, African, Asian, and North American radio astronomy institutes. Scientific results from data presented in this publication are derived from the following EVN project code: EA063

² <http://bessel.vlbi-astrometry.org>

Table 1. Parameters of EVN observations. The coordinates are given for the brightest spot.

Name	RA (h : m : s)	Dec (° : ' : ")	Phase calibrator	Synthesized beam (mas × mas; °)	RMS noise (mJy beam ⁻¹)
G78.122+3.633	20:14:26.04441	41:13:32.6295	J2007+4029	4.4 × 2.9; -67	3.8
G90.925+1.486	21:09:12.97472	50:01:03.6578	J2114+4953	4.0 × 2.8; -43	3.4
G94.602-1.796	21:39:58.25505	50:14:20.9982	J2137+5101	3.7 × 2.8; -40	4.6

**Figure 1.** Spectra and light curves of the 6.7 GHz maser emission in the studied objects. Left-hand panels: maximum (orange), minimum (blue) and average (green) spectra. Right-hand panels: light curves of main features. The filled and empty symbols represent the data from the 16-m and 32-m telescopes, respectively. Typical measurement uncertainty is shown by the bar for the first data point. The vertical magenta line denotes the date of EVN observations. A dashed rectangle for G78 time series denotes zoomed-in interval showing light curve during the high-cadence observations, plotted below.

4 RESULTS

4.1 Variability

Figure 1 shows the 6.7 GHz maser spectra and the light curves of individual spectral features; in the case of similar intensity and vari-

ability patterns, only one light curve is shown. Table 3 summarizes the results of the statistical variability analysis of light curves based on the average flux density of three spectral channels centred at the peak velocity of each feature. There are the variability index, VI , which is a degree of the amplitude variations, fluctuation index, FI ,

Table 2. Observing parameters with the Irbene 32-m and 16-m radio telescopes.

Parameter	32-m	16-m	Unit
System temperature	28 – 32	32 – 36	K
Half power beam-width	6	12	arcmin
Number of spectral channels	4096	4096	
Correlator bandwidth	1.5625	1.5625	MHz
Velocity range	35	35	km s ⁻¹
Correlator resolution	0.017	0.017	km s ⁻¹
RMS noise	0.9	1.9	Jy
Calibration accuracy	–	~20	%

Table 3. Variability properties of selected features.

V_p (km s ⁻¹)	S_p (Jy)	VI	FI	χ_r^2	$\chi_{99.9\%}^2$
G78.122+3.633 (Time-span = 2023 d, N=880)					
-4.9	10.4	0.76	0.71	9.77	1.15
-5.4	7.0	0.81	0.68	8.25	
-6.1	27.7	0.24	0.20	0.61	
-6.7	29.1	0.74	0.67	11.66	
-7.0	18.4	0.62	0.64	4.87	
-7.7	24.1	0.97	2.48	65.51	
-8.3	9.7	0.82	0.74	8.76	
G90.925+1.486 (Time-span = 1823 d, N=305)					
-69.2	61.49	0.36	0.44	3.99	1.27
-70.4	29.79	0.37	0.39	1.6	
G94.602–1.796 (Time-span = 1963 d, N=351)					
-40.9	5.30	0.14	0.45	0.68	1.25
-43.7	3.74	0.43	0.47	0.59	

measuring the spread about the mean flux density and χ^2 -test giving a probability for the presence of variability. More details on the definitions of these parameters are given in Appendix A.

All the features in G78, except for the -6.1 km s⁻¹ feature, are moderately or highly variable. The feature at -7.7 km s⁻¹ has the highest variability indices (Table 3). It initially had a flux density of 32 Jy but decayed to ~ 1.5 Jy after 1.6 yr and remained at a noise level over ~ 1.5 yr, then increased to 105 Jy at the end of our monitoring. The other variable features essentially show a similar pattern of variability. The -6.1 km s⁻¹ feature decreased by about 25 per cent on a timescale of 5.5 yr, which is marginally above the measurement accuracy. The high cadence observations after MJD 59045 revealed, for the variable features, the occurrence of flux fluctuations by a factor of 0.7–3.5 on a timescale range of 9–40 d imposed on the overall growth of flux on a timescale of 2.2 yr. We conclude that the fluctuations are real because their amplitudes are well above the measurement uncertainty. The Lomb-Scargle periodogram analysis (Scargle 1982) showed no statistically significant periodicity. These relatively rapid fluctuations are simultaneous within 3–4 d.

The two main features in G90 are moderately variable (Table 3). A likely flare occurred around MJD 58250 when the flux density increased by a factor of two during 58 d, but the flare profile could not be determined due to a gap in observations. One can only notice that the flux density has returned to a pre-flare level after 7.5 months. Since MJD ~ 58570 the emission shows an overall decrease by a factor of 1.5 during ~ 3 yr. There are similar changes in the intensity of the two features on timescales 3–11 months, but their amplitudes are within or below uncertainty in the absolute flux density calibration.

The emission of G94 is faint and not significantly variable within the noise.

4.2 Maser structure

The total intensity (0-th moment) maps of cloudlets for G78 are shown in Fig. C1, while those of the G90 and G94 sources are displayed in Figs. C9 and C12, respectively. The positions of the brightest spot of each target are listed in Table 1. The maps of spot distribution and the spectra are presented in Figure 2. The parameters of maser cloudlets are given in Tables 4, 5 and 6. In this paper, a maser *cloudlet* is defined as a group of maser spots, with a signal-to-noise ratio higher than 10, in at least three adjacent spectral channels which coincide in position within half of the synthesized beam (Bartkiewicz et al. 2020). By fitting the Gaussian function to the spectral shape of the emission of individual cloudlet we obtained the amplitude (S_{fit}), the full width at half maximum (FWHM) and the peak velocity (V_{fit}). The projected linear size of cloudlet (L_{proj}) is estimated as the distance between two of the furthest spots. The velocity gradient (V_{grad}) is estimated when a regular increase or decrease in velocity occurs, and it is defined as a maximum difference in the velocity between spots divided by their distance. Similar to Moscadelli et al. (2011a), we neglect the gradient sign for analysis. The directions of V_{grad} are given by the position angle (PA) of the cloudlet major axis measured from the blue- to red-shifted wing taken as positive if increasing to the east. Note we used flux-weighted fits for PA estimation.

G78. 98 maser spots with a velocity ranging from -8.37 to -4.77 km s⁻¹ are detected in 14 cloudlets, forming three clusters, which fall within a region of ~ 290 mas $\times 150$ mas (480 au $\times 250$ au) (Fig. 2, Table 4). The overall maser distribution is very similar to that observed 8–15 yr ago (Moscadelli et al. 2011a; Surcis et al. 2014).

Most cloudlets usually show the linear or arched distribution of spots with an internal gradient of velocity with the position. Cloudlets 5 and 6 are complex with double Gaussian profiles and curved velocity gradients (see Figs. C6 and C7). In further analysis, their components are considered separately. The angular extent of cloudlets ranges from 0.5 to 7 mas, and the average value corresponds to $L_{\text{proj}} = 4.2 \pm 0.3$ au. The velocity gradient ranges from 0.05 to 0.45 kms au⁻¹ and the average value is 0.14 ± 0.03 kms au⁻¹. The mean FWHM is 0.31 ± 0.02 km s⁻¹. We were searching for relationships between cloudlet parameters but found a moderate correlation only between L_{proj} and S_{fit} ($r = 0.596$, $p < 0.015$). Comparison of the EVN and Irbene spectra indicates that ~ 57 per cent of the emission is resolved out.

Figure 3 shows the map of cloudlets with the velocity gradient directions. Here, the negative PA values of velocity gradient (Table 4) are folded into the range 0–180°. The cloudlets with a gradient amplitude greater than 0.14 km s⁻¹ au⁻¹ tend to lay in the central part of the maser distribution. They have directions approximately orthogonal to the major disc axis, but the overall distribution of PA does not follow this trend (Fig. 3), especially the cloudlets with low V_{grad} have a wide range of PA and might reflect complex kinematics of gas on a scale of 5–20 au. For the most western emission (Cloudlet 5) the direction of the velocity gradient is consistent with the proper motion vectors reported in Moscadelli et al. (2011b) and may mark an outflowing gas.

G90. The map of 47 maser spots detected in the velocity range from -71.3 to -68.3 km s⁻¹ is shown in Figure 2 and the cloudlet parameters are listed in Table 5. The dominant emission is located in two clusters about 300 au apart, the first being a blend of Cloudlets 1 and 2 and the second with Cloudlet 4. The other four cloudlets are weak and spread over a larger area; the overall size of maser distribution is ~ 160 mas $\times 90$ mas corresponding to ~ 950 au $\times 530$ au. Most cloudlets show linear morphology (Fig. C10), except for Cloudlet 1, which is slightly twisted. The double-peaked profiles are for Cloudlets 1 and

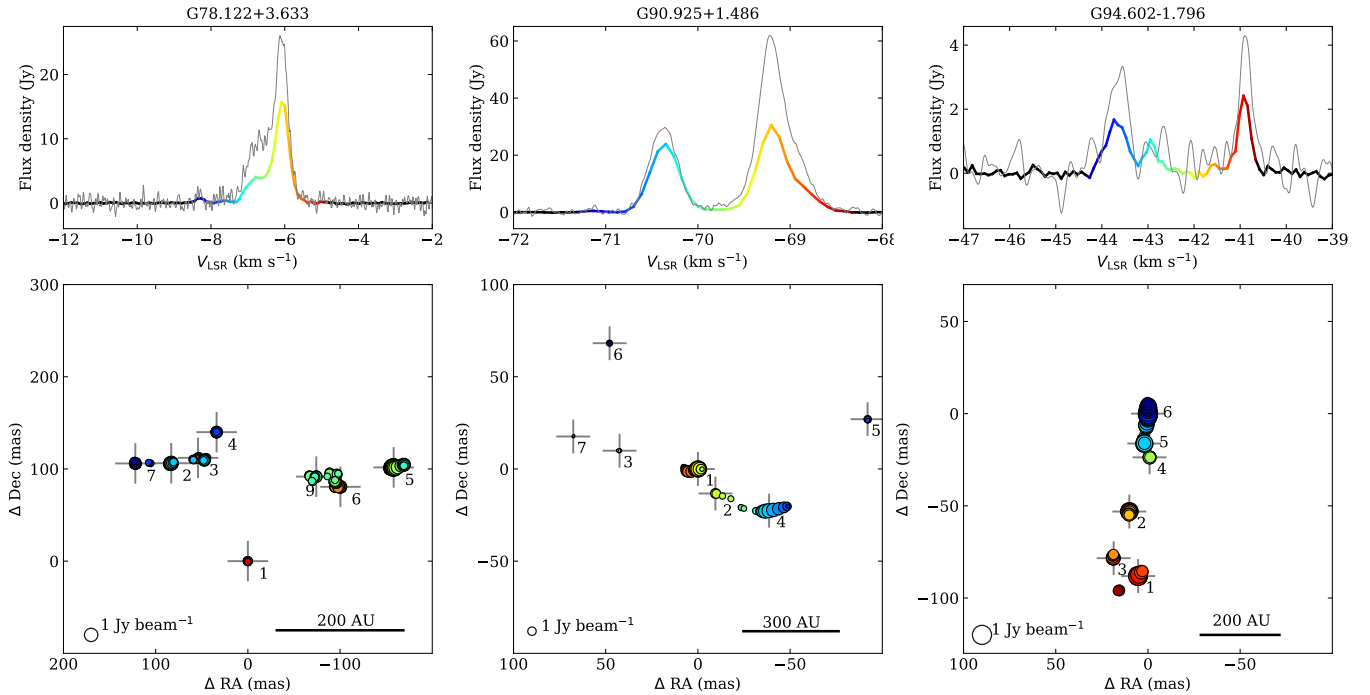


Figure 2. Top: Maser spectra of G78, G90 and G94 as obtained by EVN (colour) and the Irbene 16m radio telescope (grey line) on 31 October 2019. Bottom: Distribution of methanol maser spots. The colours are related to the LSR velocity as in the spectrum. The spot size is proportional to the logarithm of its brightness. The cloudlets (crosses) are numbered as listed in Tables 4, 5 and 6.

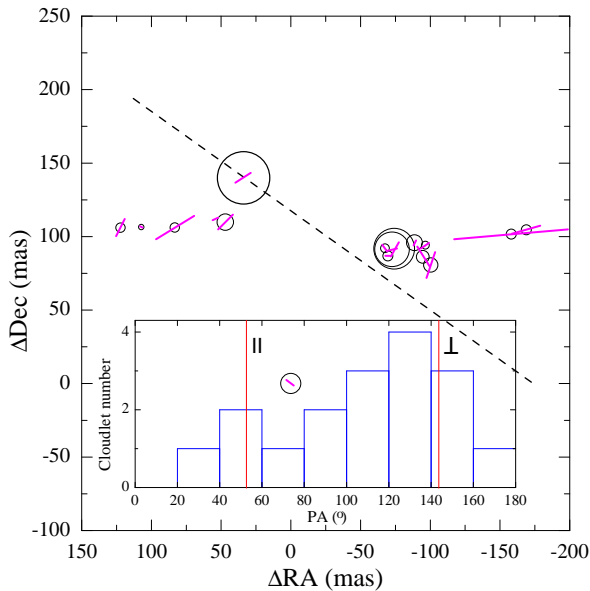


Figure 3. Map of velocity gradient directions (magenta bars) for the maser cloudlets in G78 from the 2019 EVN data. The length of the bars is proportional to the square of brightness, and the circle size is proportional to the velocity gradient. The diagonal black dashed line marks the direction of the disc plane (Cesaroni et al. 2005). The inset shows the position angle (PA) histogram of the velocity gradient; the two vertical red lines mark directions parallel and orthogonal to the plane of the disc.

2; two faint cloudlets (3 and 7) appear as incomplete Gaussians. The projected sizes of cloudlets range from 6 to 100 au, and the mean velocity gradient is $0.035 \pm 0.006 \text{ km s}^{-1} \text{ au}^{-1}$, the mean FWHM is $0.30 \pm 0.02 \text{ km s}^{-1}$. The direction of the velocity gradient of the core cloudlets at PA of $62\text{--}100^\circ$ generally follows the SW-NE elongation of maser spot distribution. The top panel of Fig. 2 shows that the emission peaked at -70.3 and -69.2 km s^{-1} is resolved out by 19 and 63 per cent, respectively, while on average 57 per cent of the flux density is missed.

G94. We found 59 maser spots that formed 6 cloudlets in the LSR velocity range from -40.5 to -44.4 km s^{-1} (Table 6). The emission is distributed over $\sim 33 \text{ mas} \times 115 \text{ mas}$ corresponding to $\sim 150 \text{ au} \times 520 \text{ au}$ (Fig. 2). There is a clear major axis of the emission structure at PA = -10° with a velocity gradient of $0.035 \text{ km s}^{-1} \text{ mas}^{-1}$ corresponding to $0.008 \text{ km s au}^{-1}$. Interestingly, the velocity gradient in the NS direction is seen in all cloudlets (Fig. C13). The cloudlet parameters are basically similar to those in the two above sources. The ratio of EVN to Irbene velocity-integrated flux density is 0.42.

5 ANALYSIS AND DISCUSSION

5.1 Variability of G78

The present study increases the number of 6.7 GHz maser maps to five acquired over 15 yr, allowing for a more detailed analysis of cloudlets variability. Previous EVN observations carried out in 2004, 2007, 2009 and 2011 were reported in Torstensson (2011), Moscadelli et al. (2011a), and Surcis et al. (2014). We retrieved the archival data for the EL032, EM064C, EM064D, and ES066E

projects³ and processed them according to the method described in Section 3. All the projects have the same observational setup, with the exception of a spectral resolution of 0.044 km s^{-1} in the 2011 experiment.

The overall maser spot distributions in the five epochs are presented in Fig. B1. Seven cloudlets persisted over 15 yr and their parameters, obtained following the procedure applied by Moscadelli et al. (2011b), are given in Table B1 and labelled in the last panel of Fig. B1. In addition to the parameters used in Table 4, we calculated the correlation coefficients of the linear fit to the spot locations on the sky plane, r_s , and the velocity changes with location, r_v , measured along the major axis of the spot distribution. Figs. C2–C8 show seven persistent cloudlets’ structures and spectra representing a wide range of morphology and intensity variations. Cloudlet 1 (Fig. C2) is the most compact (~ 1 mas) in all five epochs, and consequently, some of its parameters (r_s , r_v , V_{grad} and PA) are poorly determined. In Cloudlet 2 the brightest spots form a linear structure with high values of r_s , r_v , and steady ($\pm 10^\circ$) PA (Fig. C3). Cloudlet 3 (Fig. C4) experienced significant changes in morphology and intensity from compactly distributed 3 spots in 2004 to the complex structure and double profiles since 2009. Cloudlet 4 (Fig. C5) is compact, and its parameters are uncertain similar to Cloudlet 1. The high-velocity spots of Cloudlet 5 (Fig. C6) form a uniquely stable curved distribution over 15 yr. The low-velocity emission of Cloudlet 5 that appeared in 2009 preserved a stable linear morphology in the two consecutive observations. This cloudlet is the nearest one to the outflow traced by the 22 GHz water masers (Moscadelli et al. 2011a), and the PA of the velocity gradient direction is nearly the same as that of the outflow direction. We note that variations of intensity of Cloudlet 5 significantly deviate from a general trend observed for all the rest cloudlets for which a maximum occurred in the 2009 epoch. This suggests that the behaviour of this cloudlet is less dependent on the activity of powering HMYSO. Cloudlet 6 has a complex and twisted morphology on ~ 15 mas scale with double-peaked profile (Fig. C7) and shows strong variability. Comparing maps from 2011 to 2019 may suggest a fragmentation of this cloudlet as new closely located cloudlets (9; 11; 13 and 14) appeared. Cloudlet 7 has had an arched structure since 2007 of ~ 3 mas in size, evolving towards less curvature. We conclude the morphology and intensity of seven persistent cloudlets show significant variability on ~ 2 –15 yr timescales.

In addition to the seven persistent cloudlets, there were 28 transient cloudlets in this, as many as 22 only in one epoch. Eleven of these short-lived cloudlets had no Gaussian profile, which may be because the VLBI telescope only detects the most compact parts of low-brightness masing gas. Figure 4 presents the distribution of the cloudlets where the symbol size denotes the number of epochs in which the emission was detected. It is striking that short-lived cloudlets lie to the north of or in the three main regions of persistent emission but not to the south. Cloudlets 4 and 5 have dominant contributions to the most and least variable spectral features, respectively, and are marked in Fig. 4 with the letters H and L. The 6.7 GHz maser emission regions partly overlap with the CH_3CN ($J = 12-11$, $K=3$) emission zones for which the excitation temperature is 133 K, while south of these zones, higher excitation CH_3CN lines occur (Cesaroni et al. 2014, their Fig. 5). We, therefore, conclude that the transient emission avoidance zone is a simple consequence of the increase in the kinetic temperature, which is consistent with the standard methanol maser model (Cragg et al. 2002)

Comparison of the auto and cross-correlation spectra shows that

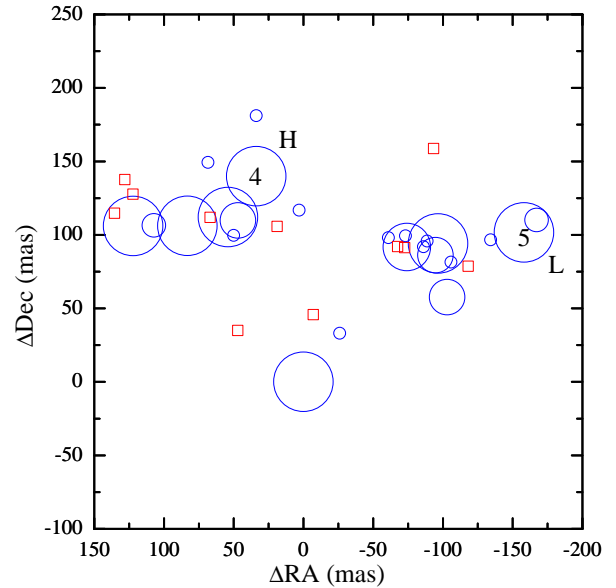


Figure 4. Map of maser cloudlets detected with five epoch EVN observations in 2004–2019 interval in G78. The symbol size is proportional to the number of epochs in which the cloudlet appeared. The blue circles and red squares mark the cloudlets with and without Gaussian profiles, respectively. Cloudlets 4 and 5 (Table 4) identified with the spectral features showing the highest and lowest variability evaluated from χ_r^2 (Table 3) are labelled with H and L, respectively.

50–60 per cent of flux density is missed with the EVN beam, which is similar to that reported for a large sample of masers (Bartkiewicz et al. 2016). The variability indices of S_{fit} for the persistent cloudlets on 15 yr timescale (Table B1), nevertheless, follow a general trend observed for the spectral features (Table 3) on 5.5 yr timescale. Cloudlet 5 largely contributes to the emission of the -6.1 km s^{-1} feature and is much less variable than Cloudlet 4, mainly forming the -7.7 km s^{-1} feature. This essential difference in variability of intensity and structure can be related to the location of Cloudlets 4 and 5 in a Keplerian disc and a disc-jet interface, respectively, as suggested by Moscadelli et al. (2011a).

The results of our 5 yr monitoring are consistent with those obtained in the 2009–2013 period (Szymczak et al. 2018) where the -7.7 km s^{-1} feature (Cloudlet 4) is strongly variable while that at -6.1 km s^{-1} (Cloudlet 5) is little variable if any. The 6.7 GHz spectra presented in earlier reports (Slysh et al. 1999; Goedhart et al. 2004) indicate that the object is highly variable on a time scale of up to 27 yr.

5.2 Relative proper motion in G78

We adopted the same approach as Moscadelli et al. (2011a) and used Cloudlet 2 (Table B1), with the LSR velocity of -7.1 km s^{-1} as a reference, to study the relative proper motions of methanol maser emission. The procedure was as follows: (1) we identified the cloudlets that were visible in all five epochs, (2) we checked if they showed reliable linear motions relative to Cloudlets 2, (3) finally, we derived the cloudlets’ displacements via linear fits over five epochs. The relative proper motions and their uncertainties are presented in Fig. 5 left. Our result is quite consistent with Moscadelli et al.’s result obtained from three epoch data spanning 5 yr. For both

³ <http://archive.jive.nl>

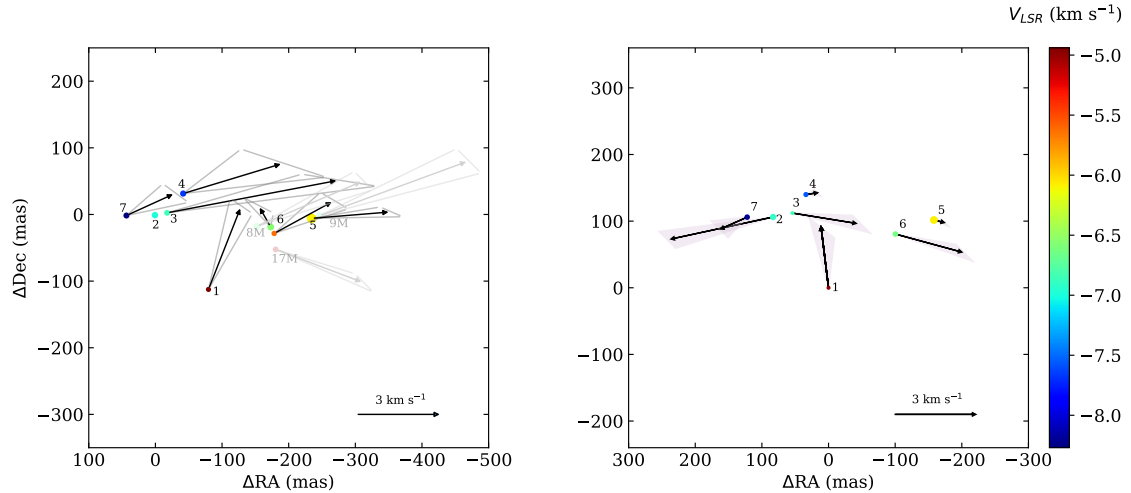


Figure 5. Relative proper motions of 6.7 GHz maser cloudlets in G78. **Left:** Results for the model of the disk-jet interface scenario by Moscadelli et al. (2011a) over a period of 2004-2019. The numbers correspond to the names of persistent cloudlets as given in Table B1. The light-coloured circles and light grey vectors correspond to features 8, 9, and 17 from Table 1 in Moscadelli et al. (2011a); they were not detected in 2011 and 2019. The grey triangles correspond to the uncertainties of proper motion vectors. **Right:** Relative proper motions derived from distance changes between cloudlet pairs as described in Section 5.2.

measurements, the velocity is in a similar range of 1.5 to 6 km s^{-1} and PA differences in the direction of proper motion vectors are less than 30° . In the eastern cluster, we noticed one more cloudlet showing proper motion, while in the western cluster, three cloudlets reported in Moscadelli et al. (2011a) disappeared. Our estimate of internal proper motion supports a view that the maser emission from the western part tracks the gas lifted from the disc near the base of outflow/jet evidenced by the 22 GHz water masers (Moscadelli et al. 2011a).

We also derived proper motions using the second method: determining the separation between cloudlet pairs. The procedure was as follows: (1) we measured relative distances between all seven cloudlets (i.e. 21 pairs) in all five epochs assuming that Cloudlet 1 is at (0,0) point in each epoch, (2) using the least squares method, we fitted linear motions for each pair to obtain the relative motions of each cloudlet within this pair (which means six vectors for each cloudlet), (3) we calculated the sum of all vectors for each cloudlet to obtain the proper motion. These results are presented in Fig. 5 right. Cloudlet 1 moves towards the remaining cloudlets, similar to the results using the above-mentioned method, while Cloudlets 2 and 7 move away from Cloudlets 3 and 4 and the western two cloudlets. The cloudlets located at the northern edge of distribution (Cloudlets 4, 5 and 7) have velocities smaller than 1 km s^{-1} , i.e. significantly lower than the rest of cloudlets lying closer to the deriving star, which is placed $\sim 400 \text{ au}$ to the south (Cesaroni et al. 2013). This picture is thus not consistent with the postulated dichotomy in the disc and disc-jet maser cloudlets (Moscadelli et al. 2011b); it may reflect the perturbed spatial-kinematic structure of disc clearly seen in the CH_3CN line maps (Cesaroni et al. 2014).

5.3 Structure and variability of G90 and G94

The overall structure of the maser in G90 is similar to that obtained in 2012 during the BeSSeL⁴ survey using VLBA. The velocity and

position of our Cloudlets 1, 2, 4 and 6 coincide with those given in the BeSSeL dataset. The rest cloudlets were not detected in 2012, likely due to a two times higher angular resolution than ours. The JVLA observation in 2012 (Hu et al. 2016) revealed the emission over $\sim 300 \times 600 \text{ mas}$ ($\sim 1700 \times 3500 \text{ au}$) region indicating the presence of extended emission resolved by the VLBA and EVN. The emission at -70.3 km s^{-1} (mainly Cloudlet 4) preserved its morphology over 7 yr. For the other cloudlets, we note a difference in PA of velocity gradient direction of less than 40° . We conclude the morphology of the source has not changed significantly on 7 yr timespan.

VLBI data for G90 implies that the emission of variable feature peaked at -69.2 km s^{-1} comes from Cloudlet 1 (the origin of the map in Fig. 2), whereas the less variable feature at -70.4 km s^{-1} is identified with Cloudlet 4. Our monitoring data indicate that for both features, low amplitude variations (20–50 per cent) on timescales of 2–3 months are tightly correlated, and the same is seen in variability on a timescale of 4 yr. Comparison with the monitoring data in the period 2009-2013 (Szymczak et al. 2018) implies the same trends in the variability of the two features. Inspection of the maser spectra available in the literature (Szymczak et al. 2000, 2012, 2018; Hu et al. 2016; Yang et al. 2019) and these obtained with the Irbene telescopes reveals that the ratio of peak flux density of features -70.4 and -69.2 km s^{-1} monotonically decreases from 2.5 to 0.4 between 1999 and 2022 (Fig. 6). As the 6.7 GHz maser line is radiatively pumped (Cragg et al. 2002), the occurrence of synchronised variations by a factor of up to 3.8 in timescales from ~ 3 months to a few years suggests global changes in the infrared photon flux driven by a central HMSYO. Figure 6 depicts that the -70.4 km s^{-1} feature rises very slowly (0.75 Jy yr^{-1}) in 2008-2022, whereas the -69.2 km s^{-1} emission exponentially rise ~ 7 times over ~ 23 yr. We hypothesise this long-term variability can be caused by changes in the amplification path length due to large-scale motions of the gas (Caswell et al. 1995) in spiral arms within the accretion disc (Bayandina et al. 2019).

The maser spectrum of G94 in the studied period changed significantly compared to that observed in 2009–2013 (Szymczak et al. 2018; Hu et al. 2016); the emission from -43.2 to

⁴ <http://bessel.vlbi-astrometry.org/>

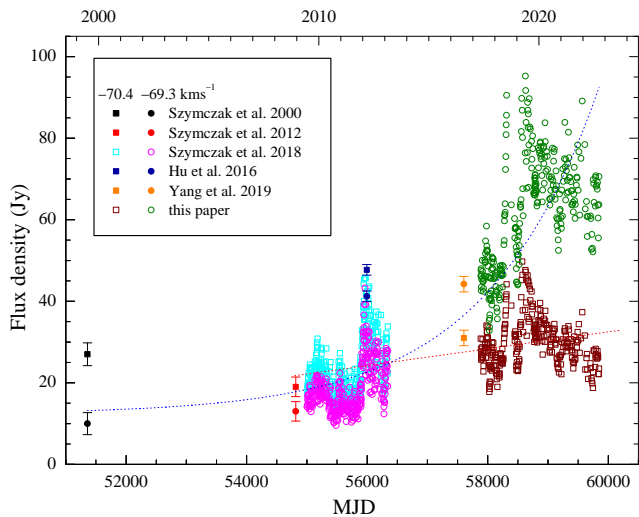


Figure 6. Long term variations of the peak flux density of the -70.4 and -69.3 km s^{-1} features in G90 marked as squares and circles, respectively. The flux calibration accuracy is ~ 10 per cent for the MJD 55005–56340 data and ~ 20 per cent after MJD 57885. The red and blue dotted lines mark the best fits of linear ($r=0.46$, $p<0.001$) and exponential ($r=0.80$, $p<0.001$) curves to the -70.3 and -69.3 km s^{-1} time series, respectively.

-42.2 km s^{-1} decreased by a factor of two. The shape of the spectrum is also significantly different from those observed ~ 20 – 24 yr ago (Slysh et al. 1999; Szymczak et al. 2000). We conclude the methanol maser shows appreciable variability on a two-decade timescale; it also displays low amplitude variability on shorter (>0.5 – 2 yr) timescales (Szymczak et al. 2018) that was not seen in the present study likely due to low sensitivity.

G94 was observed with the VLBA (BeSSeL) in December 2012 and 12 spots imaged correspond to our Cloudlets 1, 2, 3, 5 and 6 given in Table 6. As the spectral resolution of VLBA data was 0.36 km s^{-1} we cannot uncover the cloudlet’s morphology but note the same overall linear structure of 430 au with a pronounced velocity gradient in the N–S direction ($\text{PA}=170^\circ$). We have attempted to identify the brightest spots in the 2012 and 2019 VLBI data at the same velocity in order to determine the relative motion. At both epochs, the brightest blue- and red-shifted spots have velocities of -42.94 and -40.78 km s^{-1} , respectively. There is no change in the distance between the spots higher than 0.85 mas. Observations with the VLA-C in March 2012 revealed a very similar morphology of ~ 500 au in size (Hu et al. 2016). The maser structure uncovered in 1998, and 2000 with five EVN telescopes (Slysh et al. 2002) of 0.4 Jy beam^{-1} sensitivity was composed of five spots, which distribution is consistent with ours. We conclude the overall kinematic-spatial structure of the maser emission in G94 is preserved over ~ 21 yr. The brightness of individual cloudlets likely varies over shorter timescales as suggested by time series of maser features (Szymczak et al. 2018).

Near-infrared spectroscopy of G94 implied the fast jet/wind oriented nearly towards the observer (Murakawa et al. 2013). However, detection of a compact 0.23 and 0.52 mJy continuum emission at 5.8 and 44 GHz, respectively, with the position angle of the major axis of C-band emission of $91 \pm 71^\circ$ can indicate this object as a jet candidate (Purser et al. 2021). We note that the 5.8 GHz emission coincides within 100 mas with the maser position. The site was mapped in the 1.37 mm continuum emission with ~ 400 mas beam,

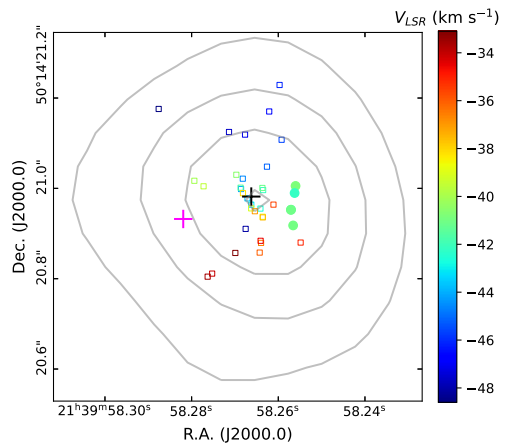


Figure 7. Map of the 1.37 mm continuum in G94 (Beuther et al. 2018). The first contour is at 4.0 mJy beam^{-1} with steps increasing by 2.0 mJy beam^{-1} . It is overlaid with the 6.7 GHz maser cloudlets (filled circles) and the peaks of the CH_3CN 220747.261 GHz line emission (open squares) retrieved from the NOEMA data (Gieser et al. 2021). The colour indicates the LSR velocity according to the scale shown in the wedge. The black and magenta crosses mark the peak of continuum emission at 5.8 and 44 GHz, respectively (Purser et al. 2021).

and four objects were found (Beuther et al. 2018). The strongest source coincides within ~ 90 mas with the 6.7 GHz maser region (Fig. 7). The NOEMA spectral line data in the 1.3 mm band (Gieser et al. 2021) allows us to retrieve the map of the CH_3CN line emission at 220747.261 GHz which is a good tracer of molecular discs (e.g. Cesaroni et al. 2014). The distribution of centroids of this thermal line emission (Fig. 7) is aligned in the N–S direction and shows a clear velocity gradient. These are exactly the same characteristics as we observed in the 6.7 GHz methanol maser line. We conclude the maser emission probes the central parts of the western edge of the disc.

6 CONCLUSIONS

We have provided analysis of single-dish 4.5 yr monitoring observations and single epoch EVN data of 6.7 GHz methanol maser emission in three HMSFRs. For G78 source, we used the archival EVN data to study the maser structure for five epochs spanned ~ 15 yr. We conclude the following:

(i) In G78 the persistent seven maser cloudlets and spectra represent a wide range of variations in intensity and morphology; the majority of them are variable over a few years. The cloudlets associated with the region tracing disc are more variable on short (< 2 months) and 2 – 15 yr time scales than the cloudlets likely tracing the outer regions of the jet. The directions of the velocity gradient of cloudlets are largely consistent with the vectors of internal proper motion derived from 5 epoch observations spanned ~ 15 yr. There were 27 transient cloudlets lying to the north or in the persistent cloudlet regions, which may indicate unsaturated amplification.

(ii) The overall structure of maser emission in G90 is stable on 7 yr interval. Two main features exhibited remarkably different patterns of variability over ~ 23 yr; the one rises linearly at the rate of 0.75 Jy yr^{-1} , while the second increase exponentially by a factor of seven. This long-term variability can be due to changes in the amplification path length.

(iii) Maser morphology in G94 is basically unchanged over 7 yr, while the light curve of the main two features is a blend of ~ 23 yr

lasting variations of low and high relative amplitudes of 0.52 and 5.82, respectively and ~ 3 months to a few years lasting synchronous changes of the relative amplitude 1.0–1.5. The latter is likely caused by changes in the pumping radiation flux and the former by large-scale gas motions.

ACKNOWLEDGEMENTS

We thank a referee for their comments and suggestions, which improved the manuscript. We thank Dr. Luca Moscadelli from INAF-Osservatorio Astrofisico di Arcetri, Italy, for the valuable discussion about proper motion analysis. This publication has received funding from the European Union's Horizon 2020 research and innovation program under RadioNet grant agreement No 730562. I.S. acknowledges support from the ERDF project "Physical and chemical processes in the interstellar medium", No.1.1.1.1/16/A/213. A.B. and her Torun collaborators acknowledge support from the National Science Centre, Poland, through grant 2021/43/B/ST9/02008.

DATA AVAILABILITY

EVN data are available at <http://archive.jive.nl>. The single-dish data presented in the paper will be shared on reasonable request to the corresponding author.

REFERENCES

- Aberfelds A., Shmeld I., Berzins K., 2018, in Tarchi A., Reid M. J., Castangia P., eds, IAU Symposium Vol. 336, *Astrophysical Masers: Unlocking the Mysteries of the Universe*. pp 277–278, doi:10.1017/S1743921317009437
- Aberfelds A., Steinbergs J., Shmeld I., Bartkiewicz A., 2021, *Astronomical and Astrophysical Transactions*, **32**, 383
- Aller M. F., Aller H. D., Hughes P. A., 2003, *ApJ*, **586**, 33–51
- Bartkiewicz A., Szymczak M., van Langevelde H. J., 2005, *A&A*, **442**, L61
- Bartkiewicz A., Szymczak M., van Langevelde H. J., Richards A. M. S., Pihlström Y. M., 2009, *A&A*, **502**, 155
- Bartkiewicz A., Szymczak M., van Langevelde H. J., 2014, *A&A*, **564**, A110
- Bartkiewicz A., Szymczak M., van Langevelde H. J., 2016, *A&A*, **587**, A104
- Bartkiewicz A., Sanna A., Szymczak M., Moscadelli L., van Langevelde H. J., Wolak P., 2020, *A&A*, **637**, A15
- Bayandina O. S., Burns R. A., Kurtz S. E., Shakhvorostova N. N., Val'ts I. E., 2019, *AJ*, **884**, 140
- Beuther H., et al., 2018, *A&A*, **617**, A100
- Burns R. A., et al., 2020, *Nature Astronomy*, **4**, 506
- Caratti o Garatti A., et al., 2017, *Nature Physics*, **13**, 276
- Caswell J. L., Vaile R. A., Ellingsen S. P., 1995, *Publ. Astron. Soc. Australia*, **12**, 37
- Cesaroni R., Felli M., Testi L., Walmsley C. M., Olmi L., 1997, *A&A*, **325**, 725
- Cesaroni R., Neri R., Olmi L., Testi L., Walmsley C. M., Hofner P., 2005, *A&A*, **434**, 1039
- Cesaroni R., et al., 2013, *A&A*, **549**, A146
- Cesaroni R., Galli D., Neri R., Walmsley C. M., 2014, *A&A*, **566**, A73
- Choi Y. K., Hachisuka K., Reid M. J., Xu Y., Brunthaler A., Menten K. M., Dame T. M., 2014, *ApJ*, **790**, 99
- Clarke A. J., Lumsden S. L., Oudmaier R. D., Busfield A. L., Hoare M. G., Moore T. J. T., Sheret T. L., Urquhart J. S., 2006, *A&A*, **457**, 183–188
- Cohen M., 1977, *ApJ*, **215**, 533
- Cragg D. M., Sobolev A. M., Godfrey P. D., 2002, *MNRAS*, **331**, 521
- Dodson R., Ojha R., Ellingsen S. P., 2004, *MNRAS*, **351**, 779
- Durjaz M., Szymczak M., Olech M., 2019, *MNRAS*, **485**, 777
- Fujisawa K., et al., 2014a, *PASJ*, **66**, 31
- Fujisawa K., et al., 2014b, *PASJ*, **66**, 78
- Fujisawa K., Yonekura Y., Sugiyama K., Horiuchi H., Hayashi T., Hachisuka K., Matsumoto N., Niinuma K., 2015, *The Astronomer's Telegram*, **8286**, 1
- Gieser C., et al., 2021, *A&A*, **648**, A66
- Goedhart S., Gaylard M. J., van der Walt D. J., 2004, *MNRAS*, **355**, 553
- Goedhart S., Maswanganye J. P., Gaylard M. J., van der Walt D. J., 2014, *MNRAS*, **437**, 1808
- Hu B., Menten K. M., Wu Y., Bartkiewicz A., Rygl K., Reid M. J., Urquhart J. S., Zheng X., 2016, *ApJ*, **833**, 18
- Keimpema A., et al., 2015, *Experimental Astronomy*, **39**, 259
- Kobak A., et al., 2023, *A&A*, **671**, A135
- MacLeod G. C., et al., 2018, *MNRAS*, **478**, 1077
- Menten K. M., 1991, *ApJ*, **380**, L75
- Minier V., Booth R. S., Conway J. E., 2000, *A&A*, **362**, 1093
- Moscadelli L., Cesaroni R., Rioja M. J., Dodson R., Reid M. J., 2011a, *A&A*, **526**, A66
- Moscadelli L., Sanna A., Goddi C., 2011b, *A&A*, **536**, A38
- Murakawa K., Lumsden S. L., Oudmaier R. D., Davies B., Wheelwright H. E., Hoare M. G., Ilee J. D., 2013, *MNRAS*, **436**, 511
- Nagayama T., et al., 2015, *PASJ*, **67**, 66
- Norris R. P., Whiteoak J. B., Caswell J. L., Wieringa M. H., Gough R. G., 1993, *ApJ*, **412**, 222
- Oh C. S., Kobayashi H., Honma M., Hirota T., Sato K., Ueno Y., 2010, *PASJ*, **62**, 101
- Olech M., Szymczak M., Wolak P., Sarniak R., Bartkiewicz A., 2019, *MNRAS*, **486**, 1236
- Olech M., Szymczak M., Wolak P., Gérard E., Bartkiewicz A., 2020, *A&A*, **634**, A41
- Olech M., Durjaz M., Szymczak M., Bartkiewicz A., 2022, *A&A*, **661**, A114
- Purser S. J. D., Lumsden S. L., Hoare M. G., Kurtz S., 2021, *MNRAS*, **504**, 338
- Reid M. J., et al., 2019, *ApJ*, **885**, 131
- Rygl K. L. J., Brunthaler A., Reid M. J., Menten K. M., van Langevelde H. J., Xu Y., 2010, *A&A*, **511**, A2
- Sakai N., Reid M. J., Menten K. M., Brunthaler A., Dame T. M., 2019, *ApJ*, **876**, 30
- Sanna A., Moscadelli L., Cesaroni R., Tarchi A., Furuya R. S., Goddi C., 2010a, *A&A*, **517**, A71
- Sanna A., Moscadelli L., Cesaroni R., Tarchi A., Furuya R. S., Goddi C., 2010b, *A&A*, **517**, A78
- Sanna A., Moscadelli L., Surcis G., van Langevelde H. J., Torstensson K. J. E., Sobolev A. M., 2017, *A&A*, **603**, A94
- Scargle J. D., 1982, *ApJ*, **263**, 835
- Slysh V. I., Val'ts I. E., Kalenskii S. V., Voronkov M. A., Palagi F., Tofani G., Catarzi M., 1999, *A&AS*, **134**, 115
- Slysh V. I., Voronkov M. A., Val'ts I. E., Migenes V., 2002, *Astronomy Reports*, **46**, 969
- Stecklum B., et al., 2021, *A&A*, **646**, A161
- Sugiyama K., et al., 2014, *A&A*, **562**, A82
- Surcis G., Vlemmings, W. H. T. van Langevelde, H. J. Moscadelli, L. Hutawarakorn Kramer, B. 2014, *A&A*, **563**, A30
- Szymczak M., Hrynek, G. Kus, A. J. 2000, *A&AS*, **143**, 269
- Szymczak M., Wolak P., Bartkiewicz A., Borkowski K. M., 2012, *Astronomische Nachrichten*, **333**, 634
- Szymczak M., Wolak P., Bartkiewicz A., 2014, *MNRAS*, **439**, 407
- Szymczak M., Olech M., Wolak P., Bartkiewicz A., Gawroński M., 2016, *MNRAS*, **459**, L56–L60
- Szymczak M., Olech M., Sarniak R., Wolak P., Bartkiewicz A., 2018, *MNRAS*, **474**, 219
- Torstensson K. J. E., 2011, PhD thesis, Leiden Observatory, The Netherlands
- Yang K., et al., 2019, *ApJS*, **241**, 18
- Zinnecker H., Yorke H. W., 2007, *Ann. Rev. Astron. Astrophys.*, **45**, 481
- Šteinbergs J., Aberfelds A., Bleiders M., Shmeld I., 2021, *Astronomical and Astrophysical Transactions*, **32**, 227

Table 4. Parameters of the 6.7 GHz methanol maser cloudlets in G78. Δ RA and Δ Dec correspond to the relative coordinates to the maser spot at RA=20^h14^m26^s05839, Dec=+41°13'32''5278 (J2000). V_p is the peak velocity, V_{fit} is the fitted velocity, FWHM is the full-width at half maximum of the Gaussian profile, S_p is the peak brightness, S_{fit} is the fitted brightness, L_{proj} is the projected linear size of cloudlet, V_{grad} is the velocity gradient and PA is the position angle of the major axis of cloudlet. Entries in italic are uncertain.

Cloudlet	Δ RA (mas)	Δ Dec (mas)	V_{fit} (km s ⁻¹)	FWHM (km s ⁻¹)	S_{fit} (Jy beam ⁻¹)	L_{proj} (mas(au))	V_{grad} (km s ⁻¹ mas ⁻¹ (km s ⁻¹ au ⁻¹))	PA (°)
1	0.0	0.0	-4.94	0.26	0.12	1.3(2.1)	0.29(0.173)	51
2	83.2	106.2	-6.93	0.33	1.38	5.5(8.8)	0.13(0.079)	122
3	54.1	112.1	-6.85	0.76	0.11	6.8(10.9)	0.10(0.064)	-65
4	33.9	139.9	-7.60	0.27	0.42	0.6(1.0)	0.72(0.451)	119
5	-168.9	104.6	-6.72	0.31	0.80	1.1(1.7)	0.14(0.085)	108
	-158.1	101.7	-6.08	0.41	8.09	6.9(11.1)	0.14(0.085)	92
6	-96.5	94.1	-6.60	0.24	0.22	1.6(2.6)	0.11(0.067)	139
	-100.4	80.6	-5.69	0.40	0.68	2.7(4.3)	0.20(0.123)	-114
7	122.1	106.0	-8.27	0.29	0.45	4.2(6.7)	0.13(0.079)	-137
8	107.2	106.5	-7.75	0.31	0.04	2.4(3.8)	0.07(0.046)	-107
9	-74.2	91.7	-6.71	0.36	0.37	0.6(1.0)	0.56(0.352)	-30
10	47.0	109.8	-7.10	0.25	0.51	1.2(1.9)	0.23(0.142)	-44
11	-94.6	86.2	-6.41	0.37	0.58	2.5(4.0)	0.17(0.109)	-133
12	-67.5	92.0	-6.70	0.33	0.17	1.4(2.2)	0.12(0.076)	45
13	-88.7	95.8	-	-	-	0.8(1.3)	0.22(0.136)	-31
14	-94.9	-80.9	-5.86	0.46	0.41	3.3(5.3)	0.11(0.066)	-67

Table 5. The same as Table 4 but for G90.925+1.486. Coordinates of the (0,0) point are RA=21^h09^m12^s97472, Dec=+50°01'03''6578 (J2000) and corresponds to the brightest maser spot.

Cloudlet	Δ RA (mas)	Δ Dec (mas)	V_{fit} (km s ⁻¹)	FWHM (km s ⁻¹)	S_{fit} (Jy beam ⁻¹)	L_{proj} (mas(au))	V_{grad} (km s ⁻¹ mas ⁻¹ (km s ⁻¹ au ⁻¹))	PA (°)
1	0.0	0.0	-69.21	0.30	21.71	2.8(12.4)	0.18(0.031)	93
	5.1	-1.4	-68.79	0.24	3.10	4.3(19.5)	0.14(0.024)	62
2	-9.5	-13.3	-69.41	0.28	1.64	0.6(3.3)	0.35(0.060)	68
	-14.1	-7.7	-69.82	0.24	0.38	1.9(11.5)	0.10(0.018)	62
3	42.5	9.9	-69.59	0.36	0.19	1.1(6.4)	0.18(0.031)	-96
4	-38.6	-22.6	-70.34	0.34	9.37	17.5(103.2)	0.05(0.008)	100
5	-92.0	27.0	-70.49	0.32	0.65	0.7(4.0)	0.29(0.050)	6
6	47.9	68.2	-71.14	0.19	0.40	0.9(5.4)	0.32(0.055)	143
7	67.6	17.6	-69.60	0.34	0.10	1.0(5.7)	0.20(0.035)	146

Table 6. The same as Table 4 but for G94.602-1.796. Coordinates of the (0,0) point are: RA=21^h39^m58^s25561, Dec=+50°14'20''9108 (J2000) and corresponds to the brightest maser spot.

Cloudlet	Δ RA (mas)	Δ Dec (mas)	V_{fit} (km s ⁻¹)	FWHM (km s ⁻¹)	S_{fit} (Jy beam ⁻¹)	L_{proj} (mas(au))	V_{grad} (km s ⁻¹ mas ⁻¹ (km s ⁻¹ au ⁻¹))	PA (°)
1	5.3	-88.1	-40.85	0.53	1.05	5.1(23.0)	0.11(0.024)	137
2	10.1	-53.1	-40.98	0.30	0.59	2.3(10.4)	0.36(0.081)	-30
	10.1	-53.7	-41.43	0.58	0.10	2.6(12.0)	0.42(0.091)	-21
3	18.6	-78.4	-41.07	0.56	0.15	2.1(9.5)	0.23(0.051)	179
4	-0.9	-23.7	-42.20	0.19	0.12	0.5(2.3)	0.43(0.96)	85
5	2.0	-16.2	-42.94	0.36	0.54	5.7(25.7)	0.14(0.031)	3
6	0.0	0.0	-43.65	0.54	0.96	14.0(63.0)	0.11(0.024)	7

APPENDIX A: VARIABILITY PARAMETERS

Statistical tools to classify significance of flux changes in light curves. Variability index (VI) (Aller et al. 2003):

$$VI = \frac{(S_{max} - \sigma_{max}) - (S_{min} + \sigma_{min})}{(S_{max} - \sigma_{max}) + (S_{min} + \sigma_{min})}. \quad (A1)$$

Here S_{max} and S_{min} are highest and lowest flux density values but σ_{max} and σ_{min} are absolute uncertainties in these measurements. VI values are in range from 0 for no variable to 1 for strongly variable lines.

Fluctuation index (FI) (Aller et al. 2003):

$$FI = \left[\frac{N}{\sum_{i=1}^N \sigma_i^2} \left(\frac{\sum_{i=1}^N S_i^2 \sigma_i^2 - \bar{S} \sum_{i=1}^N S_i \sigma_i^2}{N-1} - 1 \right) \right]^{0.5} / \bar{S}. \quad (A2)$$

Here S_i is individual flux density measured in specific epoch i , \bar{S} average flux density over the time interval under the evaluation, σ_i individual measurement uncertainties and N the number of measurements. In essence fluctuation index measures a spread around a mean value.

The reduced χ_r^2 test (Szymczak et al. 2018):

$$\chi_r^2 = \frac{1}{N-1} \sum_{i=1}^N \left(\frac{S_i - \bar{S}}{\sigma_i} \right)^2 \quad (\text{A3})$$

Provides wide range of values, for quiescent sources there will be around one and will increasing by significance of variability. For more details of methanol maser variability we suggest Goedhart et al. (2004) and Szymczak et al. (2018).

APPENDIX B: G78 EVN MULTI EPOCH

APPENDIX C: CLOUDLET STRUCTURE

This paper has been typeset from a $\text{\TeX}/\text{\LaTeX}$ file prepared by the author.

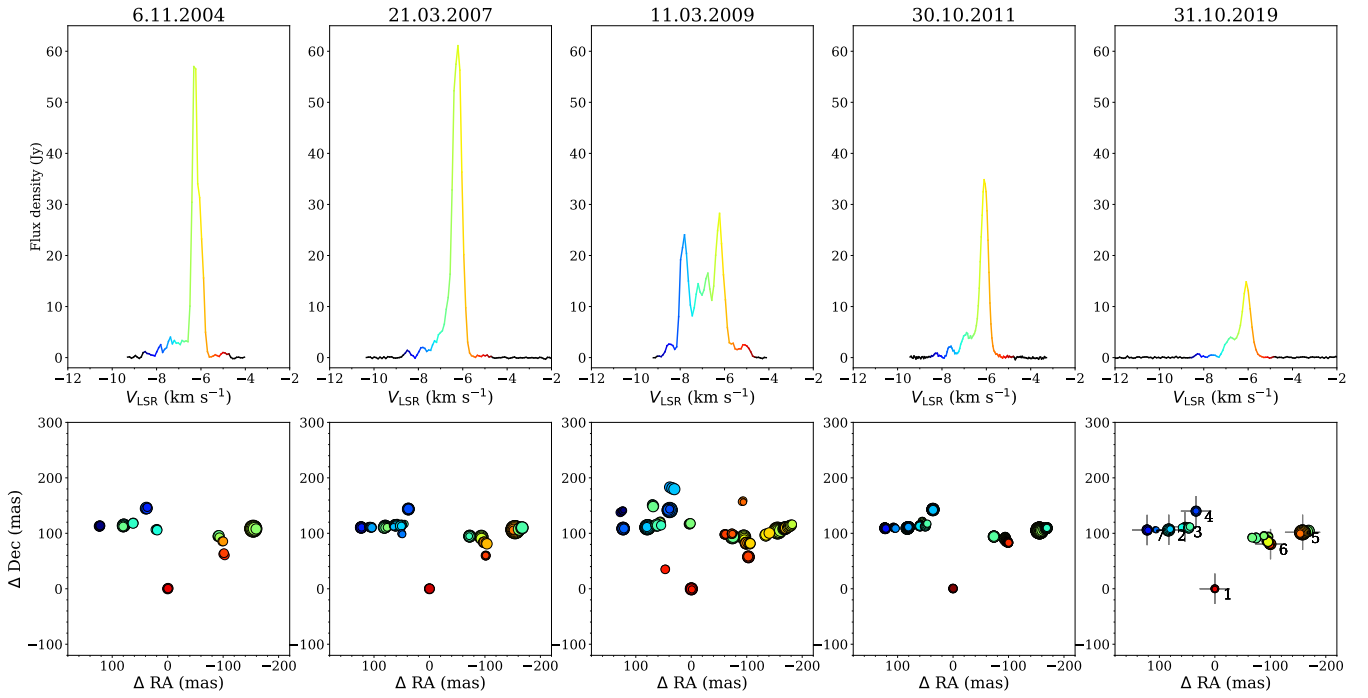


Figure B1. *Top:* The 6.7 GHz methanol maser spectra of G78.122+3.633 at five EVN epochs that were retrieved from the EVN Archive (projects EL032, EM064C, EM064D and ES066E) and our own. *Bottom:* Distributions of the methanol maser spots. The circle size represents the logarithm of its flux density and the colour corresponds to the LSR velocity as in the top panel. Coordinate centre (0,0) is the position of the spot at the LSR velocity of -4.9 km s^{-1} that was compact and stable in all epochs. Its coordinates are given in Table 4. Grey crosses and numbers on the most right panel mark positions of seven cloudlets that persisted over 15 yr.

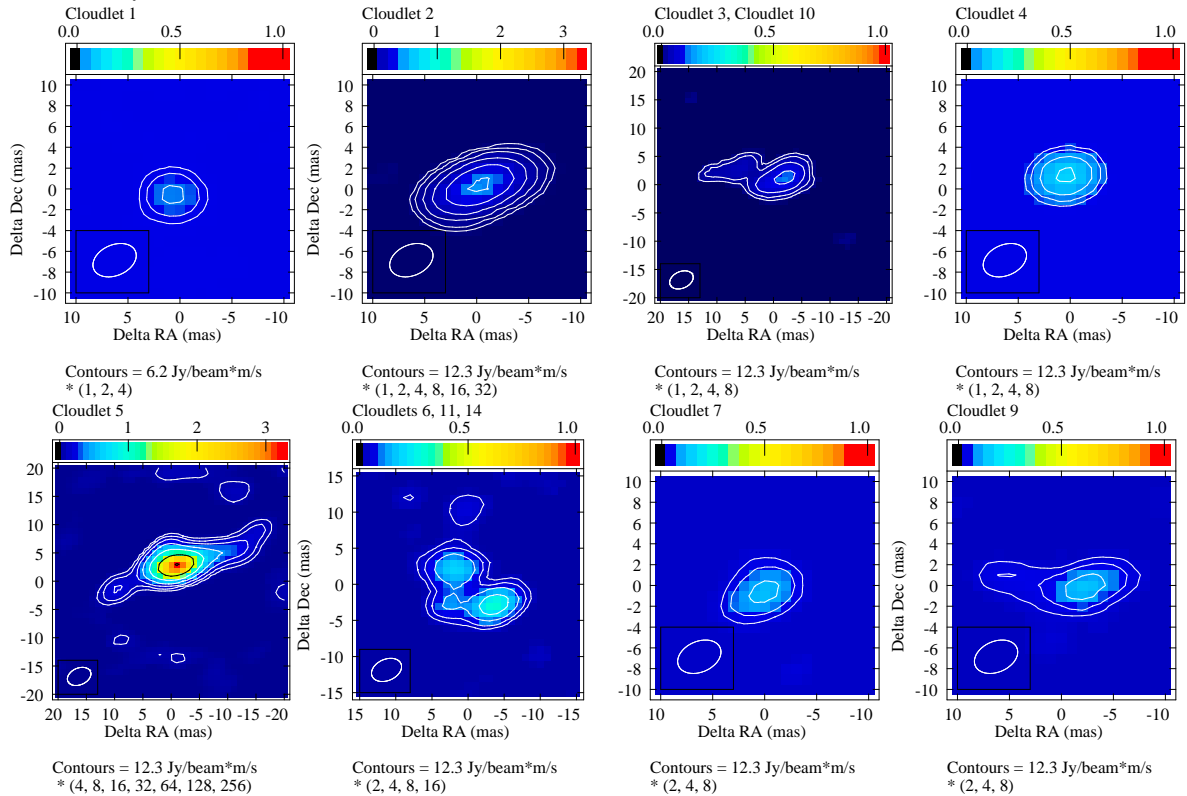


Figure C1. Total intensity (zeroth moment) maps of cloudlets in G78.122+3.633 as observed in 2019. The (0,0) point corresponds to a centre of a given cloudlet. As indicated in the top wedges, the colour scale varies linearly in $\text{Jy beam}^{-1} \times \text{km s}^{-1}$. The ellipses in the bottom left-hand corners of the images indicate the beam. Note, the panels are in different sizes to present the best resolution and contain the whole emission of each cloudlet or a group of cloudlets.

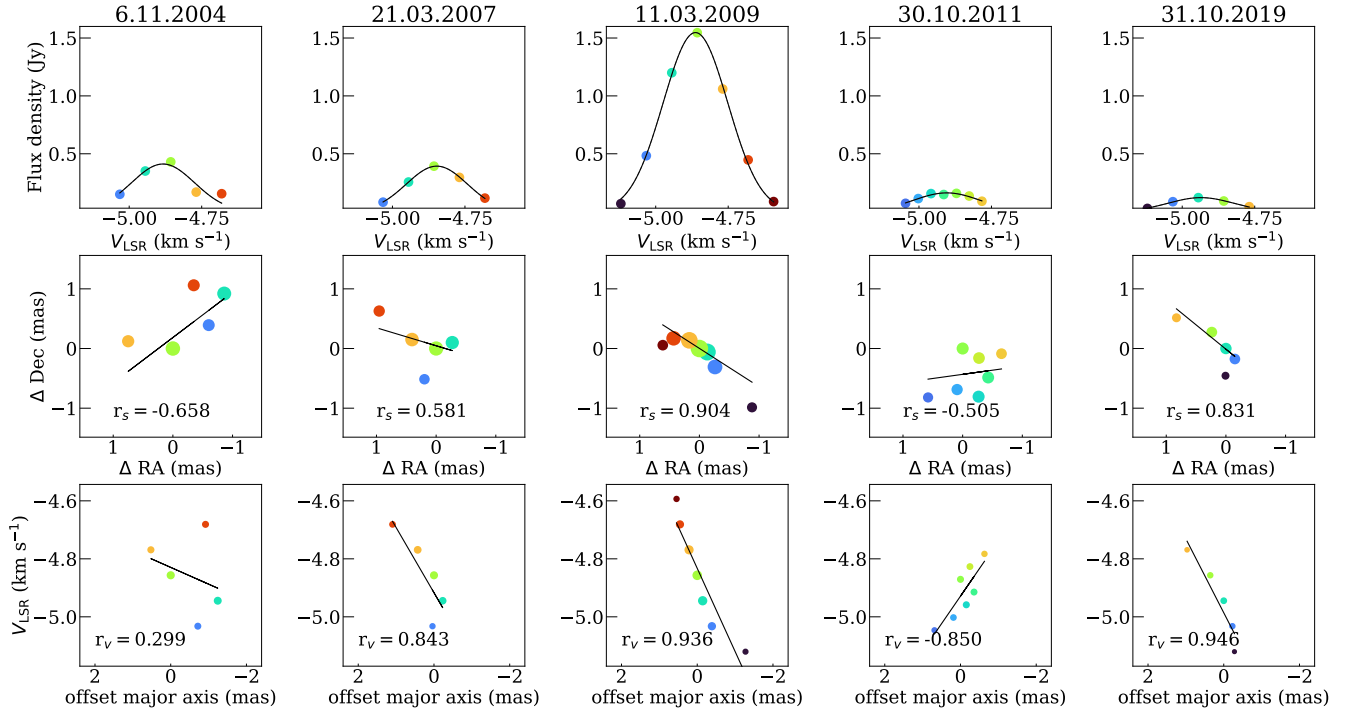


Figure C2. *Top:* Spectra of Cloudlet 1 as in Table B1 with a Gaussian velocity profile for five epochs. *Middle:* The spot distribution with the major-axis fit. A circle size is proportional to the logarithm of spot's flux density. The (0,0) point corresponds to spot position with max flux density at given epoch. *Bottom:* The spot LSR velocity vs position offset along the major axes. The correlation coefficients r_s , r_v are listed.

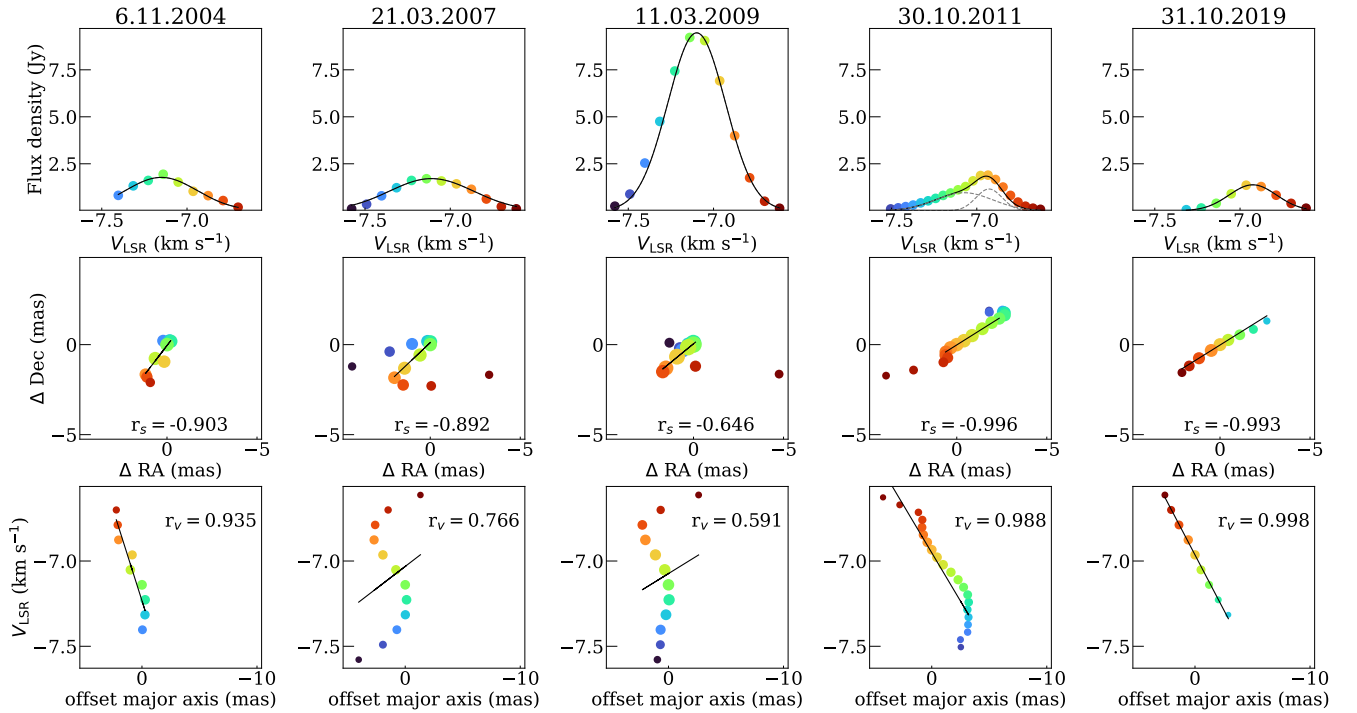


Figure C3. The same as Fig. C2 but for the Cloudlet 2.

Table B1. Parameters of the 6.7 GHz maser cloudlets in G78.122+3.633 that persisted 15 years. The parameters are the same as in Table 4 but for all five epochs. We also list the correlation coefficients of maser spot distribution (r_s) and offset of major axes (r_v) and the position angle of the major axis of maser spots within each cloudlet (PA).

Cloud Epoch	Δ RA (mas)	Δ Dec (mas)	V_{fit} (km s $^{-1}$)	FWHM (km s $^{-1}$)	S_{fit} (Jy beam $^{-1}$)	r_s	r_v	V_{grad} (km s $^{-1}$ mas $^{-1}$ (AU) $^{-1}$)	PA ($^{\circ}$)
Cloudlet 1									
2004	0.0	0.0	-4.88	0.26	0.4	-0.66	0.36	0.20(0.12)	127
2007	0.0	0.0	-4.85	0.25	0.4	0.58	0.88	0.26(0.16)	73
2009	-0.2	-0.1	-4.86	0.26	1.5	0.90	0.93	0.29(0.18)	57
2011	0.3	0.8	-4.90	0.27	0.2	-0.51	-0.92	0.18(0.12)	-82
2019	0.0	0.0	-4.94	0.26	0.1	0.83	0.95	0.28(0.17)	51
Cloudlet 2									
2004	79.3	114.4	-7.15	0.17	1.9	-0.90	0.94	0.28(0.18)	142
2007	79.7	112.4	-7.14	0.52	1.7	-0.89	0.77	0.13(0.08)	134
2009	78.6	111.2	-7.10	0.42	9.2	-0.65	0.59	0.15(0.09)	129
2011	82.3	109.4	-6.93	0.20	1.2	-0.99	0.99	0.12(0.07)	123
	-	-	-7.07	0.47	1.0	-	-	-	-
2019	83.2	106.2	-6.93	0.33	1.4	-0.99	0.99	0.13(0.08)	122
Cloudlet 3									
2004	62.4	118.0	-	-	-	-0.99	-0.90	0.26(0.16)	-29
2007	62.2	114.5	-7.00	0.43	0.9	-0.72	-0.79	0.08(0.05)	-100
2009	61.6	114.9	-6.94	0.26	1.4	-0.54	0.24	0.04(0.03)	88
	56.3	120.0	-6.56	0.23	0.5	-0.94	-0.99	0.07(0.05)	-31
2011	60.1	113.3	-7.00	0.41	0.4	-0.90	-0.90	0.19(0.12)	-53
	55.8	121.5	-6.49	0.26	0.1	-0.91	-0.97	0.04(0.03)	-26
2019	54.1	112.1	-6.85	0.76	0.1	-0.94	-0.98	0.10(0.06)	-65
Cloudlet 4									
2004	38.3	145.6	-7.67	0.29	1.1	-0.59	0.94	0.10(0.06)	109
2007	38.1	143.7	-7.64	0.29	1.1	-0.67	0.82	0.10(0.06)	99
2009	38.8	142.2	-7.73	0.28	9.2	-0.10	-0.21	0.19(0.12)	101
2011	36.3	142.9	-7.62	0.27	1.8	0.91	-0.98	0.48(0.30)	153
2019	33.9	139.9	-7.60	0.27	0.4	-0.72	0.95	0.72(0.45)	119
Cloudlet 5									
2004	-154.2	108.4	-6.10	0.33	27.8	0.80	0.97	0.11(0.07)	79
2007	-154.3	106.6	-6.09	0.36	60.7	*	0.97	0.12(0.07)	76
2009	-168.8	109.3	-6.74	0.32	2.2	-0.99	0.95	0.10(0.06)	118
	-155.6	105.0	-6.08	0.39	23.7	*	0.92	0.11(0.07)	77
2011	-168.9	109.4	-6.76	0.35	0.9	-0.99	0.75	0.09(0.05)	115
	-155.9	105.1	-6.08	0.38	26.4	0.46	0.78	0.11(0.07)	75
2019	-168.9	104.6	-6.71	0.31	0.8	-0.56	0.65	0.14(0.09)	108
	-158.1	101.7	-6.08	0.41	8.3	-0.81	0.99	0.14(0.09)	92
Cloudlet 6									
2004	-91.7	95.3	-6.64	0.32	0.6	0.38	-0.73	0.37(0.23)	97
	-98.5	85.5	-	-	-	-	-	-	-
2007	-93.8	93.4	-6.52	0.33	2.9	0.62	0.99	0.11(0.07)	-128
	-98.1	83.8	-5.49	0.45	0.5	0.67	0.79	0.28(0.18)	70
2009	-94.7	93.4	-6.52	0.30	4.2	0.87	-0.98	0.09(0.06)	-162
	-99.0	82.2	-5.50	0.48	1.2	-0.88	-0.97	0.27(0.17)	-72
2011	-93.4	89.8	-6.39	0.44	0.3	0.71	-0.99	0.09(0.06)	-138
	-99.0	83.1	-5.74	0.82	0.4	0.91	-0.95	0.14(0.08)	-112
2019	-96.5	94.1	-6.60	0.24	0.2	0.79	-0.94	0.11(0.07)	139
	-100.4	80.6	-5.70	0.40	0.7	0.70	-0.80	0.20(0.12)	-114
Cloudlet 7									
2004	123.1	113.0	-8.34	0.34	0.5	-0.96	0.41	0.17(0.11)	127
2007	123.2	110.5	-8.30	0.32	1.0	0.52	-0.95	0.30(0.19)	-147
2009	122.9	108.5	-8.30	0.32	2.1	0.33	-0.98	0.26(0.16)	-132
2011	122.5	109.0	-8.27	0.30	0.6	0.85	-0.99	0.15(0.09)	-140
2019	122.1	106.0	-8.27	0.29	0.5	0.87	-0.98	0.13(0.08)	-137

*The correlation coefficient is undefined because the EW spot distribution, i.e. variance of Y is zero.

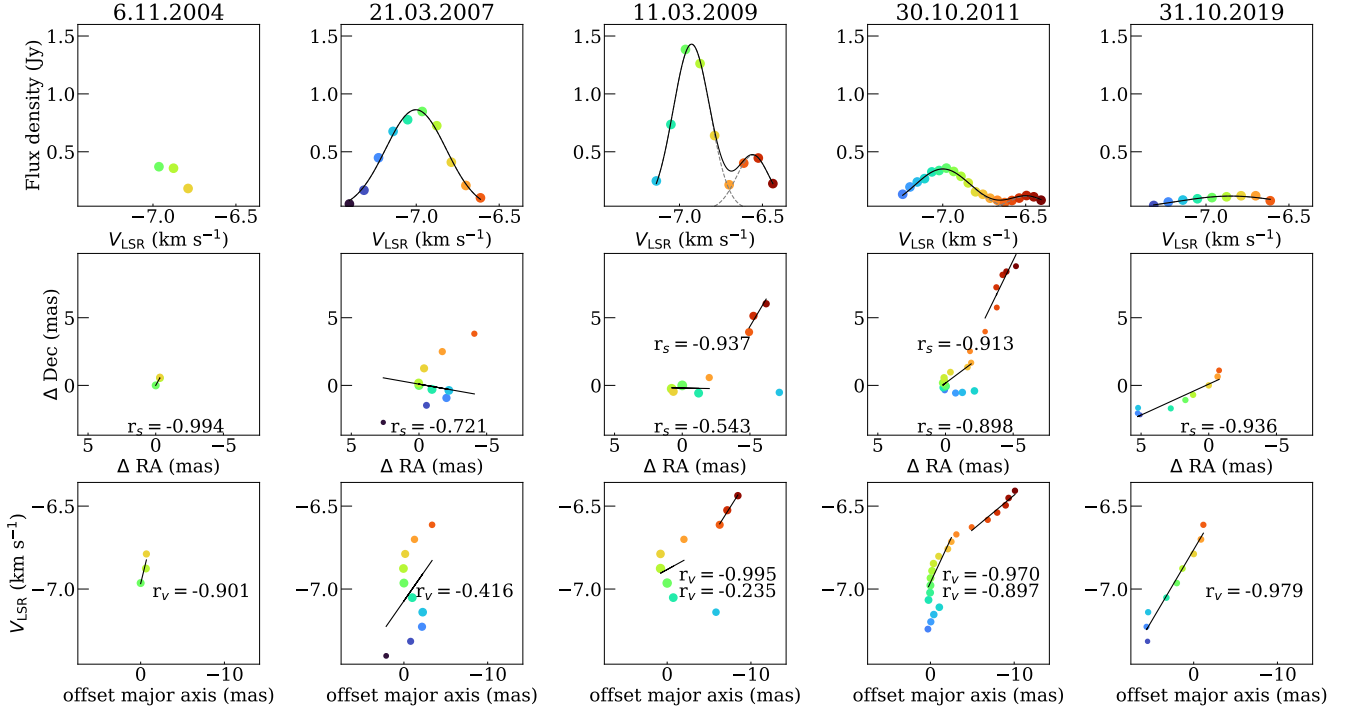


Figure C4. The same as Fig. C2 but for the Cloudlet 3.

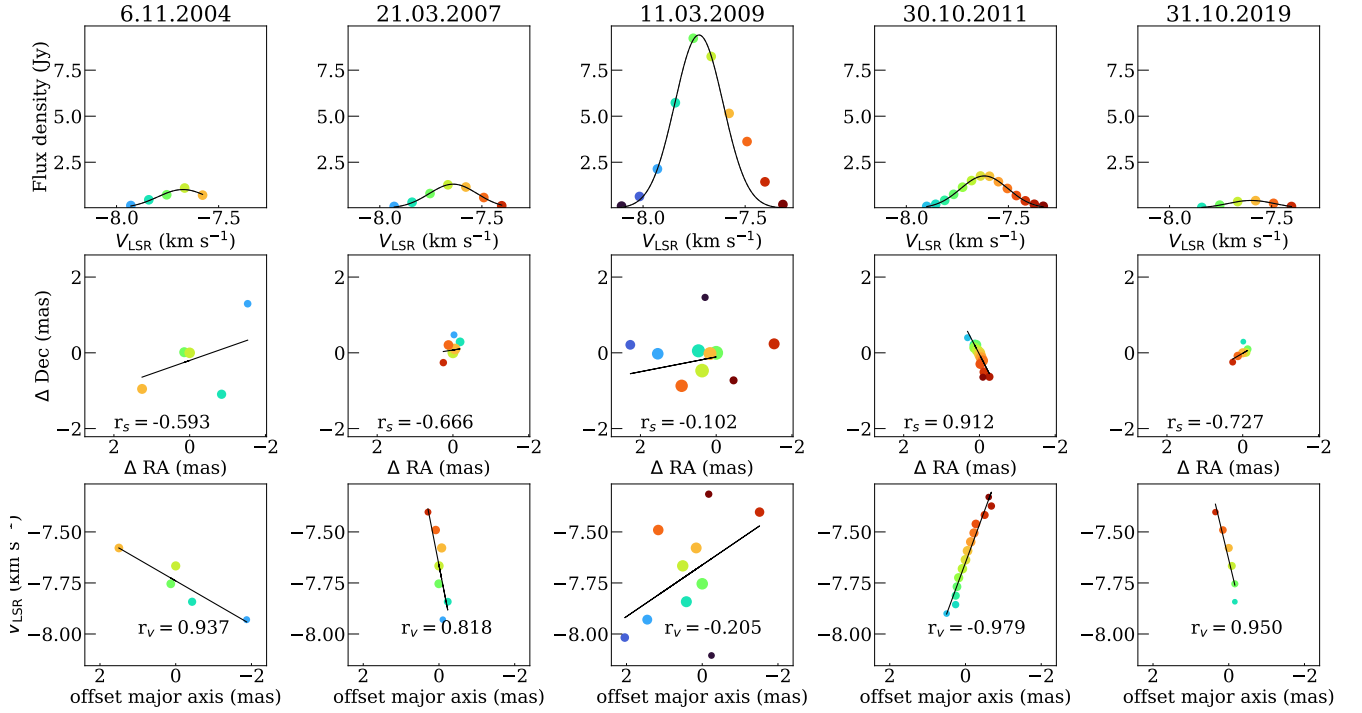


Figure C5. The same as Fig. C2 but for the Cloudlet 4.

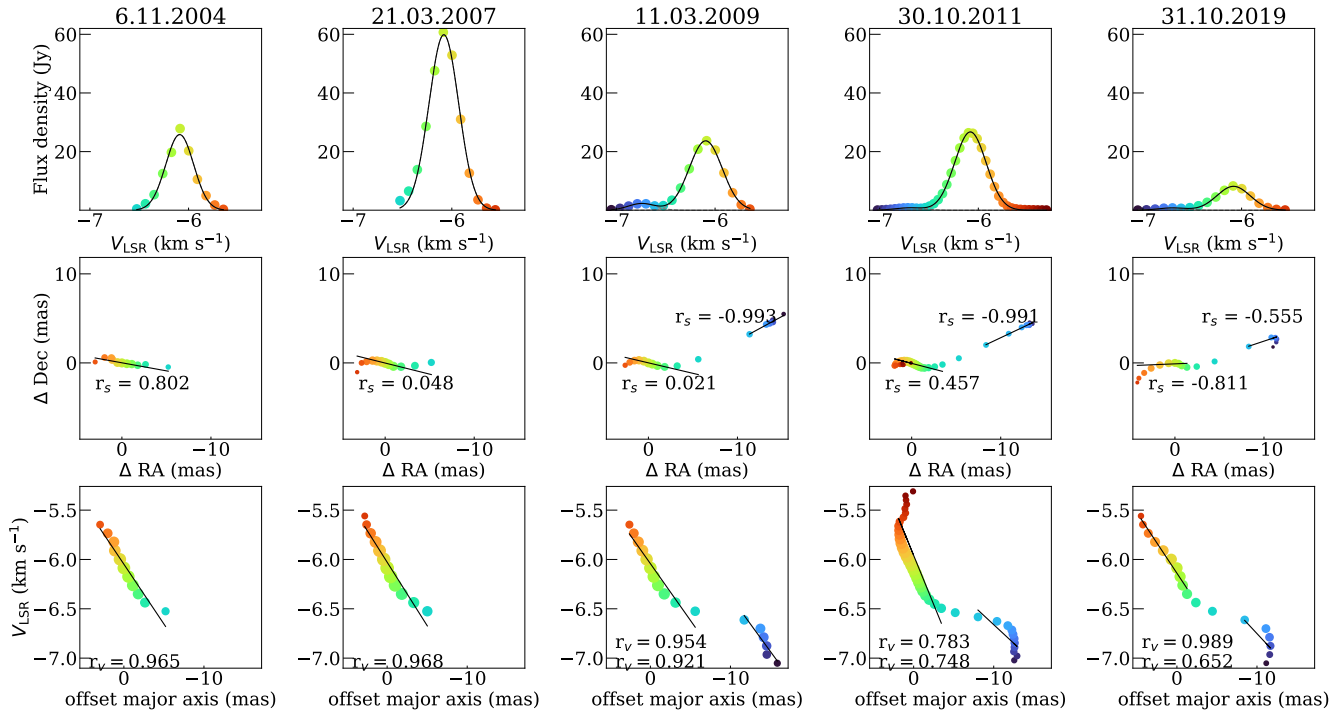


Figure C6. The same as Fig. C2 but for the Cloudlet 5.

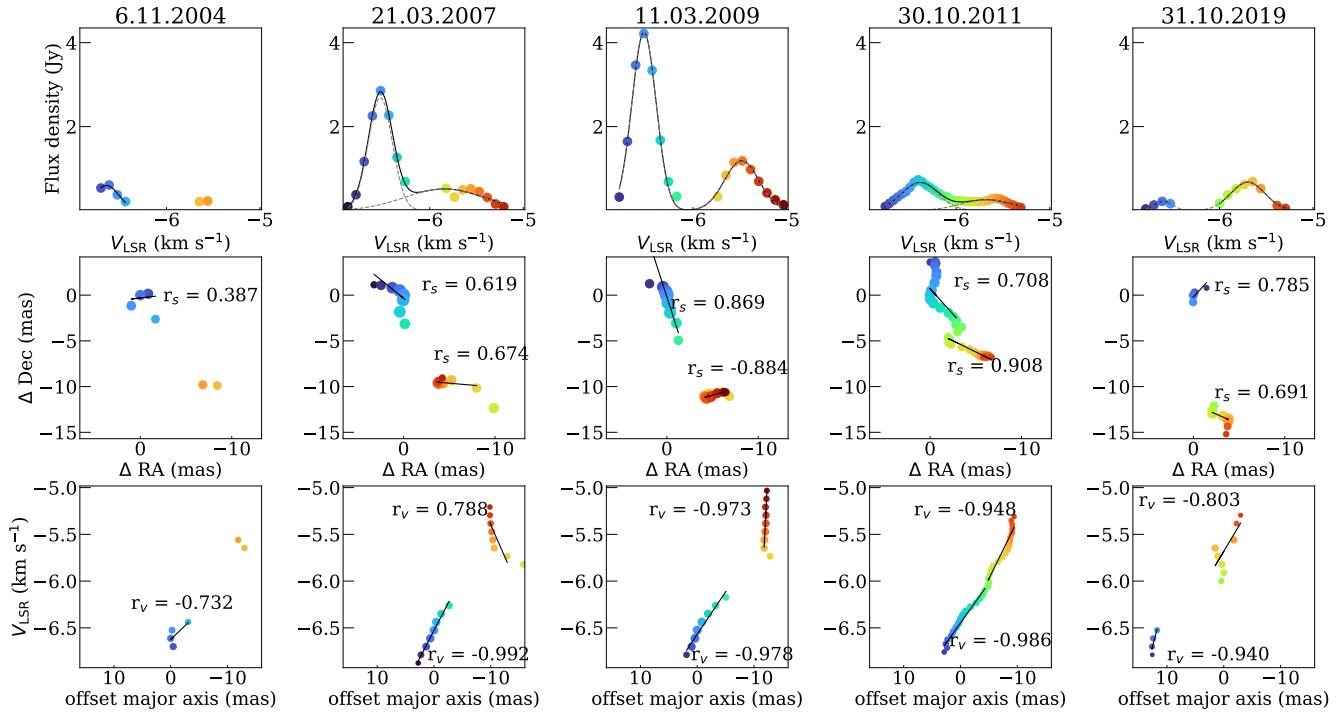


Figure C7. The same as Fig. C2 but for the Cloudlet 6.

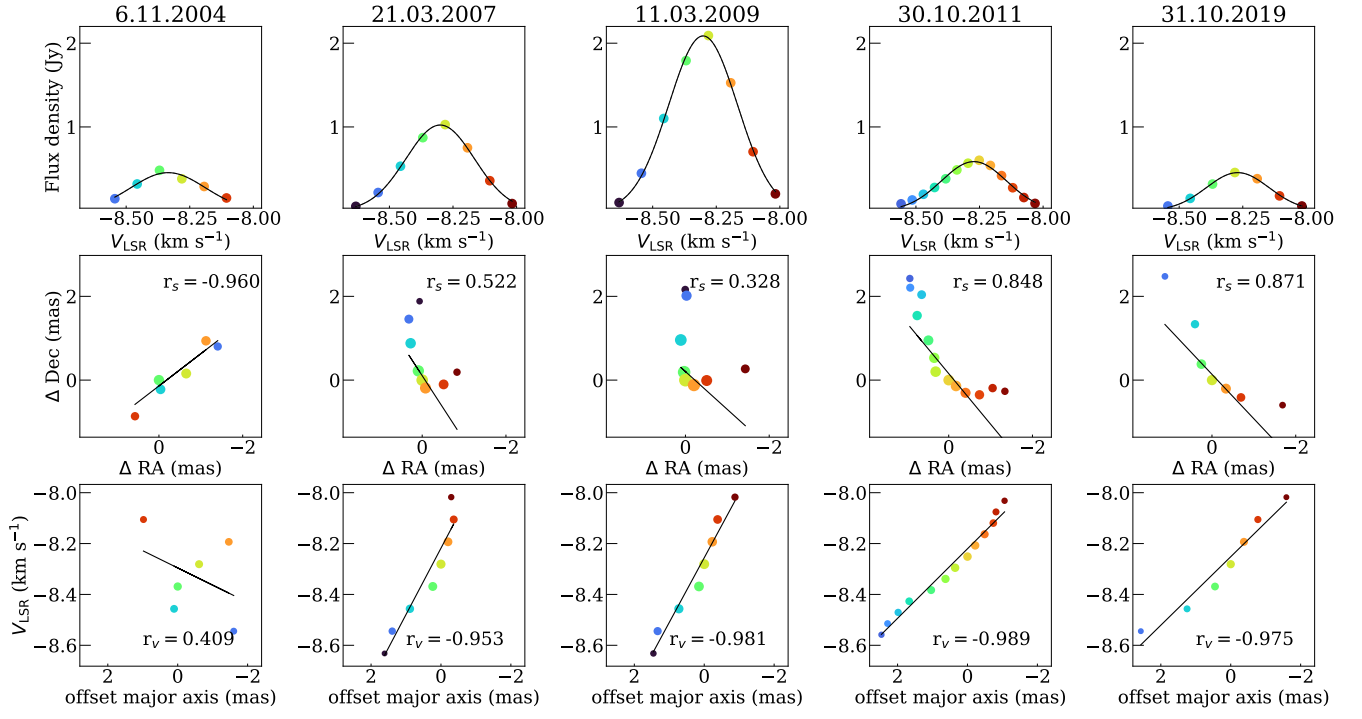
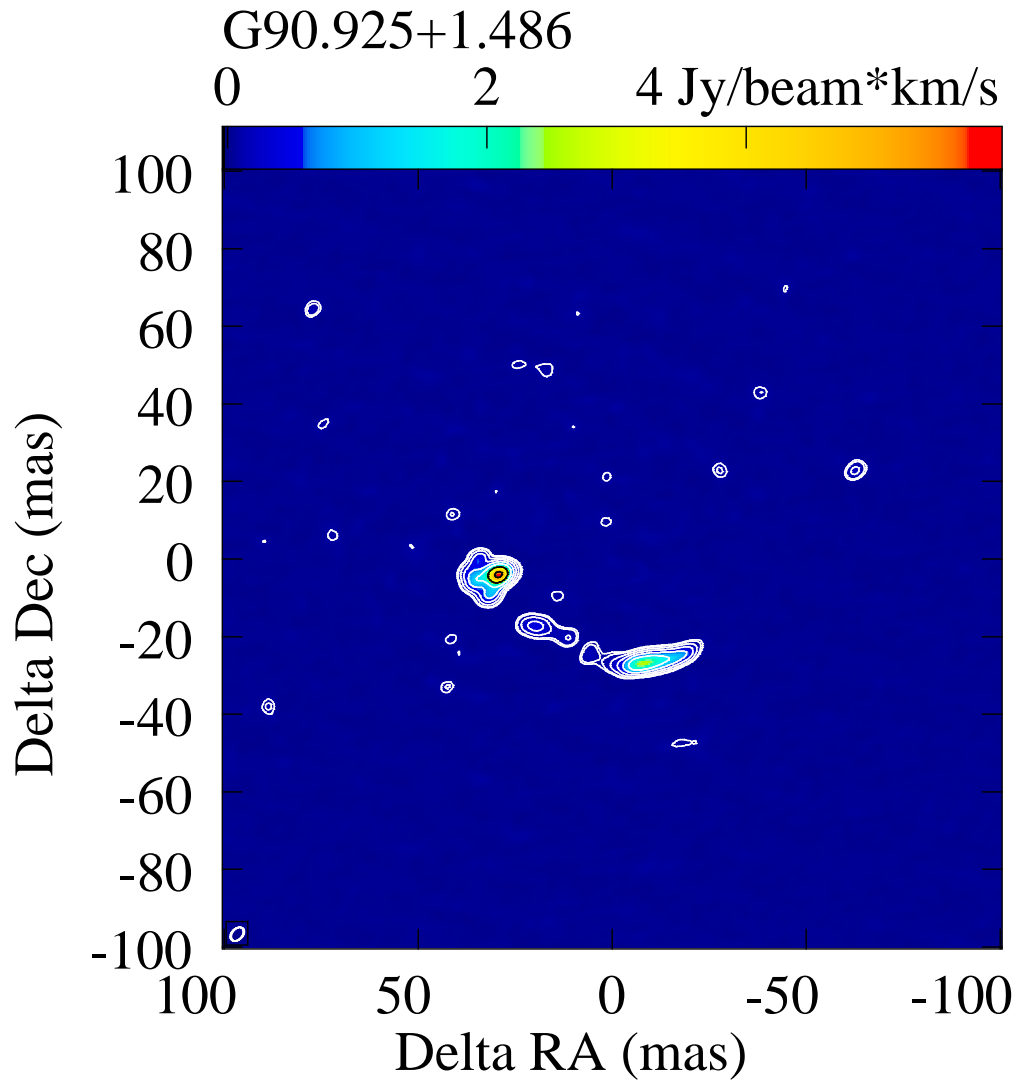


Figure C8. The same as Fig. C2 but for the Cloudlet 7.



Contours = 20.38 Jy/beam*m/s
 * (3, 4, 8, 16, 32, 64, 128, 256)

Figure C9. Total intensity (zeroth moment) map of G90. The ellipse in the bottom left-hand corner of the images indicates the beam.

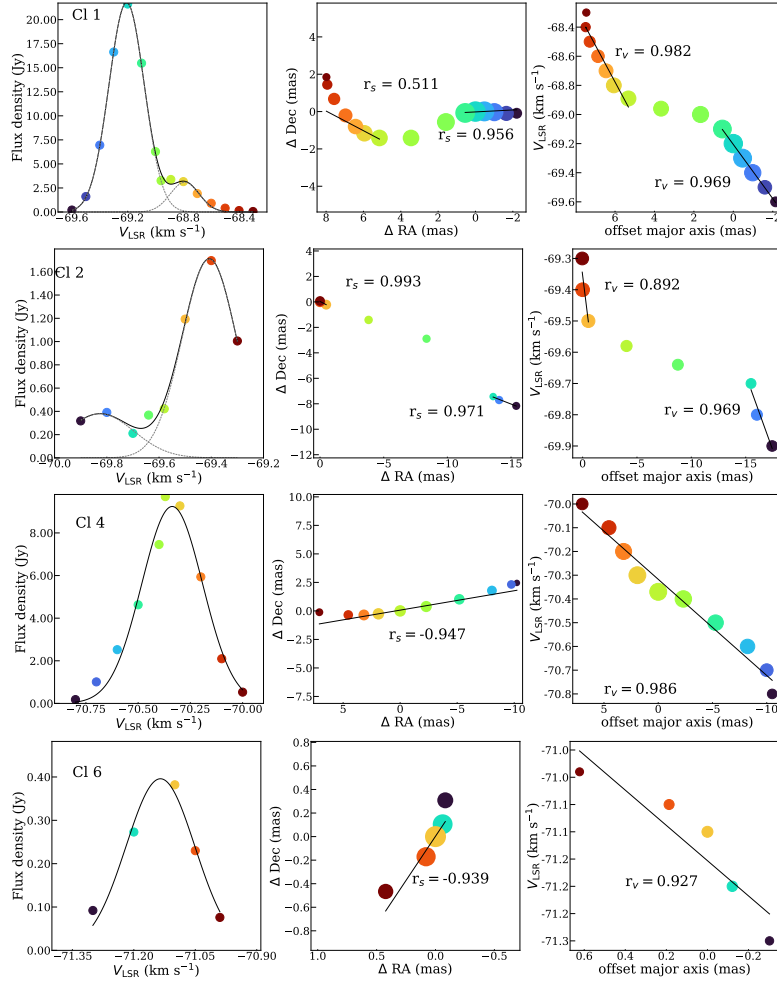


Figure C10. Cloudlets of G90.925+1.486, as obtained in the EVN observation in 2019. The same information as in Fig. C2 (but panels are orientated horizontally now). We show cloudlets 1, 2, 4, and 6, since 3, 5 and 7 structures are very simple.

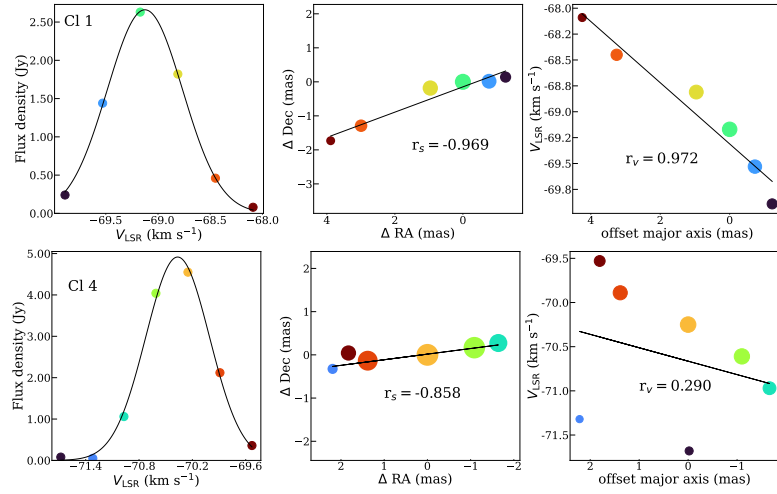


Figure C11. Cloudlets of G90.925+1.486 as obtained by the BeSSeL team. The same information as in Fig. C10.

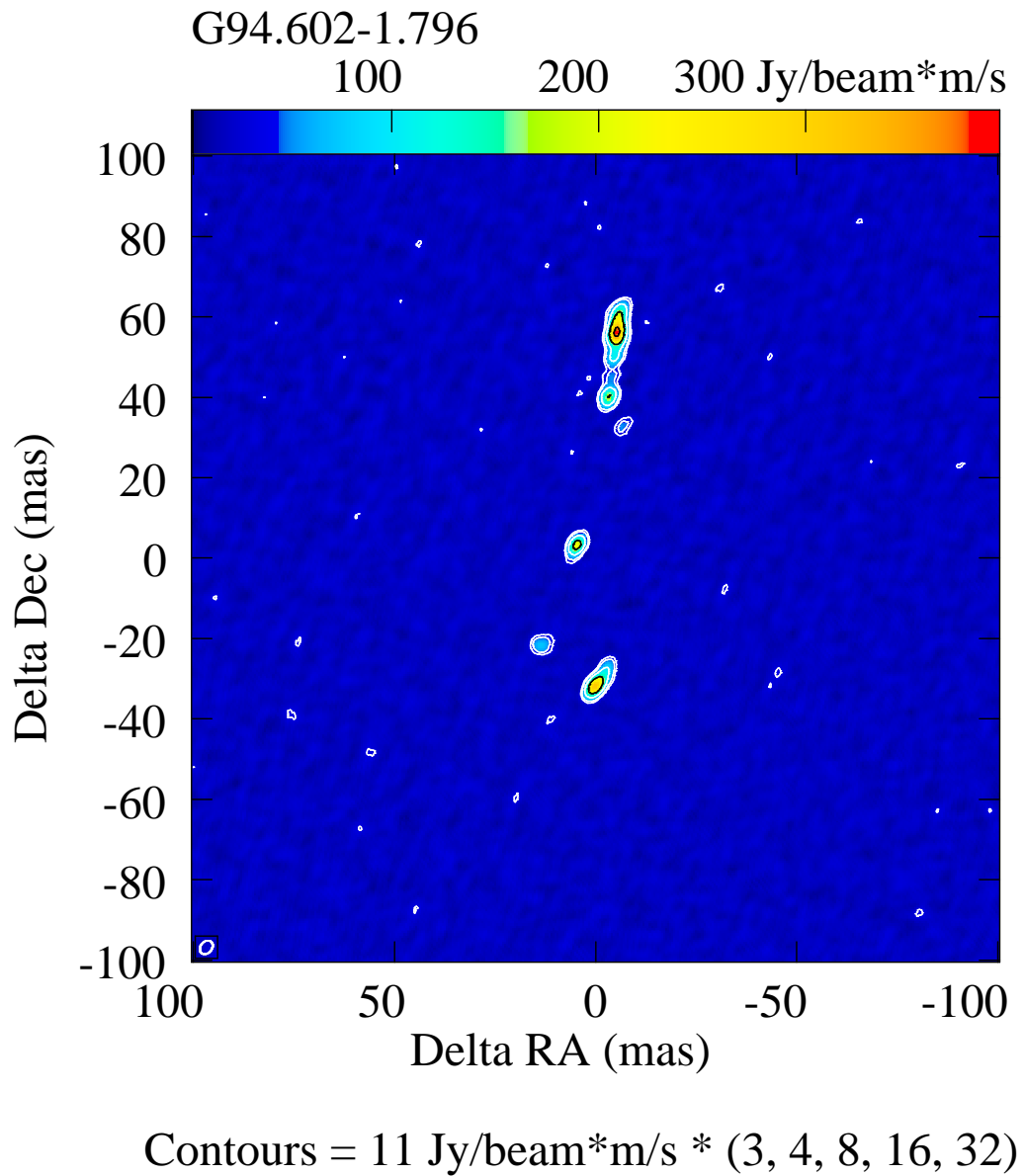


Figure C12. Total intensity (zeroth moment) map of G94. The ellipse in the bottom left-hand corner of the images indicates the beam.

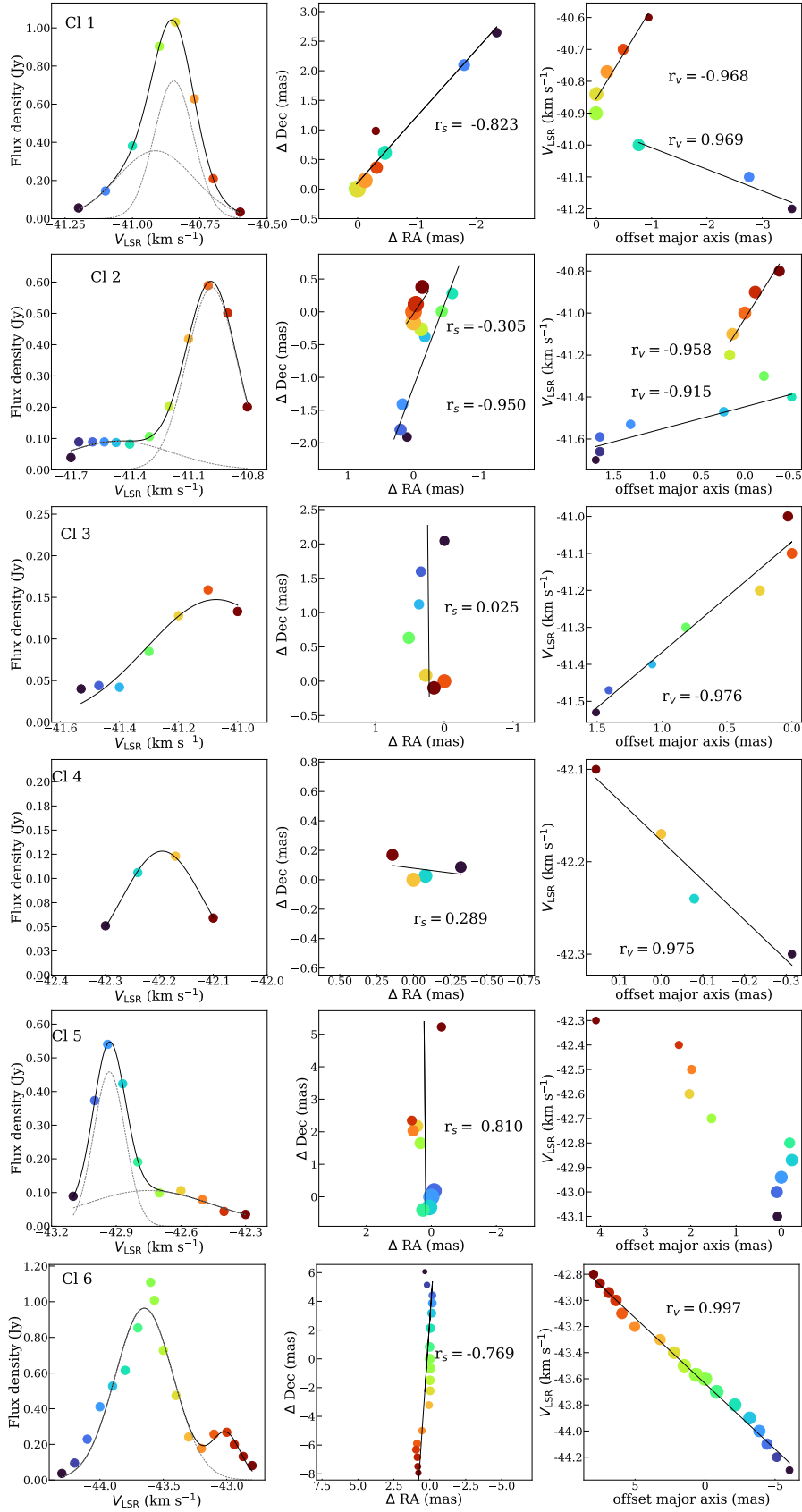


Figure C13. Cloudlets of G94.602–1.796 as obtained in the EVN observation in 2019. The same information as in Fig. C10.